

## RESEARCH ARTICLE

# Aerodynamic model identification of an autonomous aircraft for airborne wind energy

Giovanni Licitra<sup>1</sup>  | Adrian Bürger<sup>2</sup> | Paul Williams<sup>3</sup> | Richard Ruitkamp<sup>3</sup> | Moritz Diehl<sup>1</sup>

<sup>1</sup>Department of Microsystems Engineering, University of Freiburg, Freiburg im Breisgau, Germany

<sup>2</sup>Faculty of Management Science and Engineering, Karlsruhe University of Applied Sciences, Karlsruhe, Germany

<sup>3</sup>Ampyx Power B.V., The Hague, The Netherlands

## Correspondence

Giovanni Licitra, Department of Microsystems Engineering, University of Freiburg, 79110 Freiburg im Breisgau, Germany.

Email: gianni.licitra7@gmail.com

## Present Address

Giovanni Licitra, Georges-Köhler-Allee 102, 79110 Freiburg im Breisgau, Germany.

## Funding information

FP7-ITN-TEMPO, Grant/Award Number: 607 957; H2020-ITN-AWESCO, Grant/Award Number: 642 682; Federal Ministry for Economic Affairs and Energy via eco4wind and DyConPV; Deutsche Forschungsgemeinschaft, Grant/Award Number: Research Unit FOR 2401; State Ministry of Baden-Wuerttemberg for Sciences, Research and Arts, Grant/Award Number: Az: 22-7533.-30-20/9/3

## Summary

Airborne wind energy (AWE) refers to a novel technology capable of harvesting energy from wind by flying crosswind patterns with tethered autonomous aircraft. Successful design of flight controllers for AWE systems relies on the availability of accurate mathematical models. Due to an expected nonconventional structure of the airborne component, the system identification procedure must be ultimately addressed via an intensive flight test campaign to gain additional insight about the aerodynamic properties. In this paper, the longitudinal dynamics of a rigid-wing, high lift, autonomous aircraft for AWE are identified from experimental data obtained within flight tests. The aerodynamic characteristics are estimated via an efficient time-domain multiple experiments model-based parameter estimation algorithm.

## KEYWORDS

airborne wind energy, autonomous aircraft, experimental design, large-scale optimization, system identification, parameter estimation

## 1 | INTRODUCTION

In the landscape of innovative renewable energy systems, airborne wind energy (AWE) is a novel emerging technology. The AWE promises to harvest energy from wind with both lower installation costs and higher capacity factors compared to conventional wind turbines, up to a level that could render AWE even more economically viable than fossil fuels.

Despite the fact that the idea of using tethered aircraft for wind power generation appeared for the first time in the late 1970s,<sup>1</sup> it is only in the last decade that academia and industry made substantial progress in turning the idea into a practical implementation. The postponement of AWE technology is mainly due to the significant complexities in terms of control,<sup>2</sup> modeling,<sup>3,4</sup> identification,<sup>5,6</sup> materials,<sup>7</sup> mechanics, and power electronics.<sup>8</sup> Furthermore, these systems need to fulfill high level of reliability while simultaneously operating close to optimality. Such requirements have brought many developers to the use of rigid-wing autonomous aircraft as airborne component.<sup>9-13</sup>

In the aerospace field, it is the current practice to retrieve the aircraft aerodynamic properties by a combination of wind tunnel testing, computational fluid dynamics (CFD)<sup>14</sup> analysis, and empirical methods such as DATCOM.<sup>15</sup> For standard aircraft configurations, such methods for obtaining aerodynamic characteristics are generally in agreement with those obtained via flight tests. However, empirical methods, which can provide the quickest results, tend to be less accurate and more difficult to apply to unconventional designs. The CFD is much more accurate but requires a fine mesh to capture the flow dynamics accurately, and as a consequence, it involves significant computational resources to obtain a complete aerodynamic database. As far as it regards wind tunnel experiments, they generally provide the most accurate results with a suitably-sized model that matches the Reynold's numbers of the real system. However, for unconventional systems, such approach can also be expensive. In any case, an intensive flight test campaign must be set in order to gain additional insight into the aerodynamic properties and to validate parameters on the full-scale system.

This work is entirely based on the second prototype high lift, rigid-wing autonomous aircraft designed by Ampyx Power B.V.<sup>9</sup> and shown in Figure 1.

Ampyx Power B.V. adopts the so-called *lift mode* strategy<sup>1,2,16,17</sup> where the airplane delivers a high tension on the tether, which is anchored to a ground-based generator. An artist's rendering of the two main phases of a lift mode airborne wind energy system (AWES) is shown in Figure 2.

A successful flight test campaign, which aims to identify the aerodynamic parameters of the aircraft, depends on many factors, such as selection of instrumentation, signal conditioning, flight test operations procedure, parameter estimation algorithm, and signal input design. In the work of Licitra et al.,<sup>5</sup> aerodynamic properties were estimated via flight tests with conventional maneuvers for the pitch rate dynamics, only. In another work of Licitra et al.,<sup>18</sup> optimal maneuvers were computed for the case study by solving a time-domain model-based optimum experimental design (OED) problem, which aims to obtain more accurate parameter estimates while enforcing safety constraints. The optimized inputs were compared with respect to conventional maneuvers widely used in the aerospace field and successfully tested within real experiments.<sup>19</sup> In this paper, estimation of the aerodynamic characteristics is carried out via an efficient multiple experiment, ie, multiple-experiment model-based parameter estimation (MBPE) algorithm, for dynamic systems based on *direct methods* using both conventional and optimized experiments. Data fitting is applied throughout the aircraft longitudinal dynamics using a nonlinear model structure. The presented work will be used as a guideline for the system identification of the next prototype designed by Ampyx Power B.V.<sup>9</sup> and shown in Figure 3.

This paper is organized as follows. In Section 2, the mathematical model of a rigid-wing airborne component of a generic AWES is introduced. Subsequently, a suitable model structure is selected for the estimation of aerodynamic properties augmented with model assumptions as well as neglected dynamics. Section 3 focuses on the design and evaluation of input signals. A preliminary estimation performance analysis is carried out using the Fisher information matrix and an overview of both flight test procedures and decoupling of dynamics are provided. In Section 4, the experimental data obtained from conventional and optimized flight test campaigns are presented. Section 5 formulates the MBPE algorithm,



**FIGURE 1** The second prototype high lift, rigid-wing autonomous aircraft designed by Ampyx Power B.V. [Colour figure can be viewed at [wileyonlinelibrary.com](http://wileyonlinelibrary.com)]

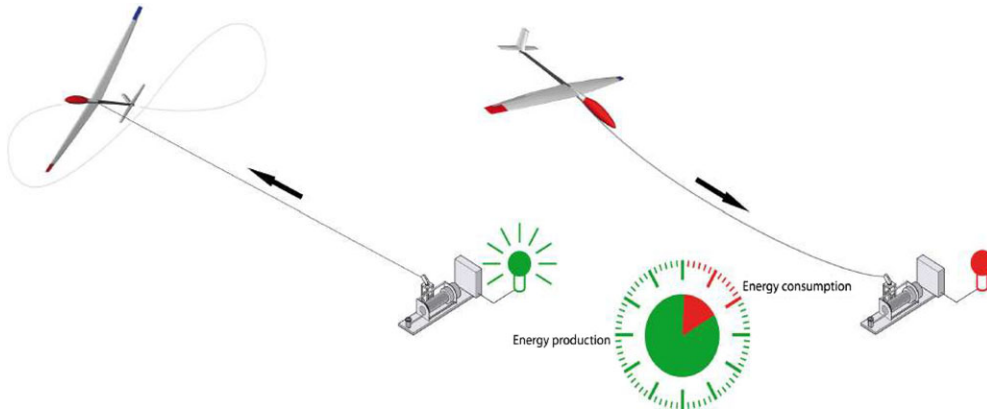


**FIGURE 2** Working principles of a lift mode AWES with a *production* and *consumption phase*. A lift mode AWES produces power by performing periodical variation of both length and tether tension. Power generation occurs during the so-called *reel-out phase*, where the tether tension is used to rotate a drum, driving an electric generator located on the ground. A *reel-in phase* is required due to finite tether length. By changing the flight pattern in such a way that less lifting force is produced, the tether can be wound up with a significant lower energy investment than what was gained in the power production phase [Colour figure can be viewed at [wileyonlinelibrary.com](http://wileyonlinelibrary.com)]

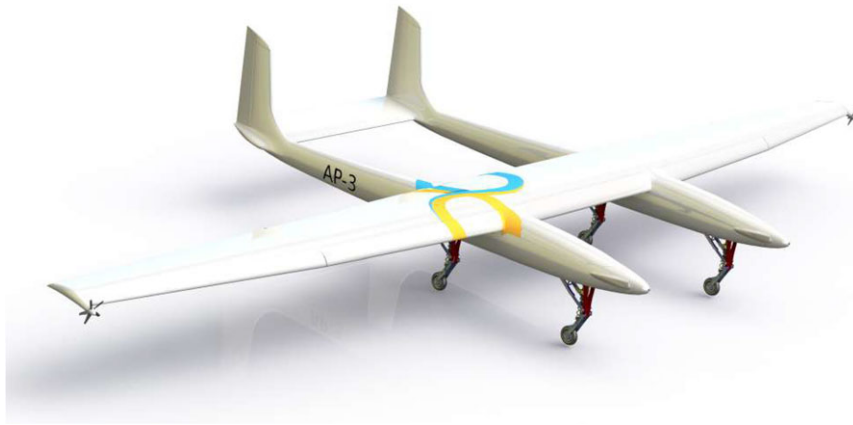


**FIGURE 3** The third prototype high lift, rigid-wing autonomous aircraft designed by Ampyx Power B.V. [Colour figure can be viewed at [wileyonlinelibrary.com](http://wileyonlinelibrary.com)]

whereas in Section 6.1, data fitting is performed on the obtained experimental data. Finally, in Section 6.2, both estimates and model validation are assessed and conclusions are provided in Section 7.

## 2 | MODELING OF A RIGID-WING AWES

In this section, a mathematical formulation of an AWES is introduced. Subsequently, a nonlinear model structure is selected for the purpose of system identification, underlying model assumptions, and neglected dynamics.

### 2.1 | Modeling of AWES in natural coordinates

A rigid-wing AWES can be efficiently modeled as a set of DAEs described by nonminimal coordinates by means of Lagrangian mechanics. The equations of motion for a tethered airborne component are given as<sup>3</sup>

$$\dot{\mathbf{p}}^n = \mathbf{R}_{nb} \cdot \mathbf{v}^b \quad (1a)$$

$$m \cdot \dot{\mathbf{v}}^b = \mathbf{f}_c^b + \mathbf{f}_p^b + \mathbf{f}_a^b + \mathbf{f}_g^b - m(\boldsymbol{\omega}^b \times \mathbf{v}^b) \quad (1b)$$

$$\dot{\mathbf{R}}_{nb} = \mathbf{R}_{nb} \cdot \boldsymbol{\Omega} \quad (1c)$$

$$\mathbf{J} \cdot \dot{\boldsymbol{\omega}}^b = \mathbf{m}_c^b + \mathbf{m}_p^b + \mathbf{m}_a^b - (\boldsymbol{\omega}^b \times \mathbf{J} \cdot \boldsymbol{\omega}^b), \quad (1d)$$

where  $\mathbf{v}^b = [u, v, w]^\top$  and  $\boldsymbol{\omega}^b = [p, q, r]^\top$  are the translational and rotational speed vector defined in body-fixed frame (denoted with the superscript  $\mathbf{b}$ ),  $\mathbf{m}$  is the mass, and  $\mathbf{J}$  is the inertia dyadic of the aircraft. In (1a), the rate of change in position  $\dot{\mathbf{p}}^n$  is defined in north-east-down (NED) frame and it is obtained by means of the direct cosine matrix (DCM) from body to NED frame  $\mathbf{R}_{nb} \in \mathbb{R}^{3 \times 3}$ , whereas (1c) is the time evolution of the DCM with  $\boldsymbol{\Omega} \in \mathbb{R}^{3 \times 3}$  being the skew symmetric matrix of  $\boldsymbol{\omega}^b$ . The aircraft is subject to forces  $\mathbf{f}_{\{c,p,g\}}^b$  and moments  $\mathbf{m}_{\{c,p,g\}}^b$  coming from the cable, propellers and gravity, whereas  $\mathbf{f}_a^b = [X, Y, Z]^\top$  and  $\mathbf{m}_a^b = [L, M, N]^\top$  denote the aerodynamic forces and moments, respectively. The mathematical formulation in (1) is extensively used for pattern generation using an optimal control approach.<sup>20,21</sup>

In order to identify the aerodynamic forces  $\mathbf{f}_a^b$  and moments  $\mathbf{m}_a^b$ , one has to either discard or have good models of the other contributions. For this application, it is convenient to perform untethered flight tests to both simplify the overall system modeling and avoid disturbances caused by tether vibrations. Furthermore, the propulsion system introduces additional noise for each angular rate and acceleration channel provided by the rotation of the blades.

Hence, a flight test campaign, which aims toward the identification of aerodynamic properties, needs to be performed without tether such that the cable does not interfere with the overall aircraft dynamics,<sup>5</sup> and additionally, propellers must be switched off whenever an excitation signal occurs in order to decouple the uncertainty in thrust effects on the aerodynamic parameter estimation, simplifying (1) to

$$\mathbf{m} \cdot \dot{\mathbf{v}}^b = \mathbf{f}_a^b + \mathbf{f}_g^b - \mathbf{m}(\boldsymbol{\omega}^b \times \mathbf{v}^b) \quad (2a)$$

$$\dot{\mathbf{R}}_{nb} = \mathbf{R}_{nb} \cdot \boldsymbol{\Omega} \quad (2b)$$

$$\mathbf{J} \cdot \dot{\boldsymbol{\omega}}^b = \mathbf{m}_a^b - (\boldsymbol{\omega}^b \times \mathbf{J} \cdot \boldsymbol{\omega}^b). \quad (2c)$$

Note that Equation (1a) is discarded since it does not provide any meaningful information for system identification purposes.

Finally, as far as it regards the cable dynamics, a comprehensive study can be found in the works of Williams et al,<sup>22,23</sup> whereas the propeller forces and moments are normally obtained via extensive test bench.

## 2.2 | Model selection

The case study considered within this work is a high lift, rigid-wing autonomous aircraft used as airborne component of a lift mode AWES designed by Ampyx Power B.V.<sup>9</sup> Details on the system can be found in the works of Ruiterkamp and Sieberling,<sup>2</sup> Licitra et al,<sup>19</sup> and Diehl et al,<sup>24</sup> whereas Table A1 collects the main physical properties.

For system identification purposes, it is more convenient to have the velocity Equation (2a) in terms of *wind-axes* variables: airspeed  $V_T$  and aerodynamic angles  $\beta$  and  $\alpha$ , which are the angle of side slip and attack, respectively. Furthermore, the aircraft attitude can be described via the Euler angles kinematics, where  $\phi$ ,  $\theta$ ,  $\psi$  denote the roll, pitch, and yaw angle. The proposed model structure is therefore given by<sup>25</sup>

$$\dot{V}_T = \frac{Y \sin \beta + X \cos \alpha \cos \beta + Z \cos \beta \sin \alpha}{m} + G_{V_T}, \quad (3a)$$

$$\dot{\beta} = \frac{Y \cos \beta - X \cos \alpha \sin \beta - Z \sin \alpha \sin \beta}{m V_T} + \frac{G_\beta}{V_T} - r \cos \alpha + p \sin \alpha, \quad (3b)$$

$$\dot{\alpha} = \frac{Z \cos \alpha - X \sin \alpha}{m V_T \cos \beta} + \frac{G_\alpha}{V_T \cos \beta} + \frac{q \cos \beta - (p \cos \alpha + r \sin \alpha) \sin \beta}{\cos \beta}, \quad (3c)$$

$$\dot{\phi} = p + r \cos \phi \tan \theta + q \sin \phi \tan \theta, \quad (3d)$$

$$\dot{\theta} = q \cos \phi - r \sin \phi, \quad (3e)$$

$$\dot{\psi} = \frac{q \sin \phi + r \cos \phi}{\cos \theta}, \quad (3f)$$

$$\dot{p} = \frac{J_{xz}}{J_x} \dot{r} - qr \frac{(J_z - J_y)}{J_x} + qp \frac{J_{xz}}{J_x} + \frac{L}{J_x}, \quad (3g)$$

$$\dot{q} = -pr \frac{J_x - J_z}{J_y} - (p^2 - r^2) \frac{J_{xz}}{J_y} + \frac{M}{J_y}, \quad (3h)$$

$$\dot{r} = \frac{J_{xz}}{J_z} \dot{p} - pq \frac{J_y - J_x}{J_z} - qr \frac{J_{xz}}{J_z} + \frac{N}{J_z}, \quad (3i)$$

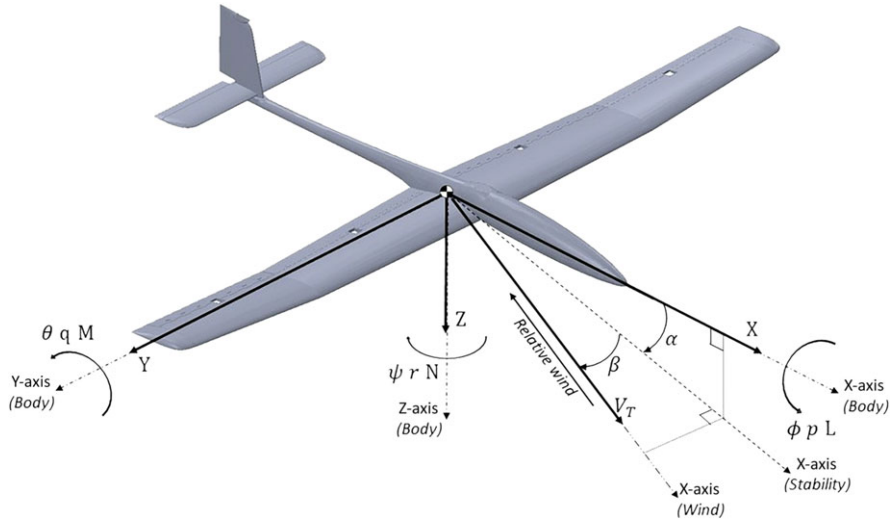


**FIGURE 4** Definition of axes, Euler angles, aerodynamic states, forces, and moments on a rigid-wing aircraft [Colour figure can be viewed at [wileyonlinelibrary.com](http://wileyonlinelibrary.com)]

where  $G_{V_T}$ ,  $G_\beta$ ,  $G_\alpha$  are the gravity components expressed in wind frame and equal to

$$G_{V_T} = g_D (\sin \beta \sin \phi \sin \theta - \cos \alpha \cos \beta \sin \theta + \sin \alpha \cos \beta \cos \phi \cos \theta), \quad (4a)$$

$$G_\beta = g_D (\cos \alpha \sin \beta \sin \theta + \cos \beta \sin \phi \cos \theta - \sin \alpha \sin \beta \cos \phi \cos \theta), \quad (4b)$$

$$G_\alpha = g_D (\sin \alpha \sin \theta + \cos \alpha \cos \phi \cos \theta), \quad (4c)$$

with  $g_D \approx 9.81 \text{ m/s}^2$  the gravitational acceleration. The nomenclature introduced previously is summarized in Figure 4.

The mathematical model (3) implicitly presumes that the vehicle is a rigid body with a plane of symmetry such that the moments of inertia  $J_{xy}$ ,  $J_{xz}$  are zero, whereas the Earth is assumed flat and nonrotating with a constant gravity field.<sup>26</sup>

Note that the model equations in (3) are also widely used for linearization purposes, dynamics analysis, and control system design.<sup>25</sup> Within this work, the aerodynamic forces ( $X$ ,  $Y$ ,  $Z$ ) and moments ( $L$ ,  $M$ ,  $N$ ) are normalized with respect to the dynamic pressure  $\bar{q} = \frac{1}{2} \rho V_T^2$  with  $\rho \approx 1.225 \text{ kg/m}^3$  being the free-stream mass density, and a characteristic area for the aircraft body

$$X = \bar{q} S C_X \quad Y = \bar{q} S C_Y \quad Z = \bar{q} S C_Z \quad (5a)$$

$$L = \bar{q} S b C_l \quad M = \bar{q} S \bar{c} C_m \quad N = \bar{q} S b C_n. \quad (5b)$$

In (5),  $S$ ,  $b$ , and  $\bar{c}$  are reference wing area, wing span, and mean aerodynamic chord, respectively, whereas  $C_X$ ,  $C_Y$ , and  $C_Z$  denote the forces, and  $C_l$ ,  $C_m$ , and  $C_n$  are the moment coefficients. For conventional aircraft, the aerodynamic coefficients are usually broken down into a sum of terms as follows:

$$C_X = C_{X_\alpha} \alpha + C_{X_{\hat{q}}} \hat{q} + C_{X_{\delta_e}} \delta_e + C_{X_0}, \quad (6a)$$

$$C_Y = C_{Y_\beta} \beta + C_{Y_{\hat{p}}} \hat{p} + C_{Y_{\hat{r}}} \hat{r} + C_{Y_{\delta_a}} \delta_a + C_{Y_{\delta_r}} \delta_r, \quad (6b)$$

$$C_Z = C_{Z_\alpha} \alpha + C_{Z_{\hat{q}}} \hat{q} + C_{Z_{\delta_e}} \delta_e + C_{Z_0}, \quad (6c)$$

$$C_l = C_{l_\beta} \beta + C_{l_{\hat{p}}} \hat{p} + C_{l_{\hat{r}}} \hat{r} + C_{l_{\delta_a}} \delta_a + C_{l_{\delta_r}} \delta_r, \quad (6d)$$

$$C_m = C_{m_\alpha} \alpha + C_{m_{\hat{q}}} \hat{q} + C_{m_{\delta_e}} \delta_e + C_{m_0}, \quad (6e)$$

$$C_n = C_{n_\beta} \beta + C_{n_{\hat{p}}} \hat{p} + C_{n_{\hat{r}}} \hat{r} + C_{n_{\delta_a}} \delta_a + C_{n_{\delta_r}} \delta_r, \quad (6f)$$

which depend on the normalized body rates  $\hat{p} = \frac{bp}{2V_T}$ ,  $\hat{q} = \frac{\bar{c}q}{2V_T}$ ,  $\hat{r} = \frac{br}{2V_T}$ , angle of attack  $\alpha$ , side slip  $\beta$ , and the control surface

deflections, which in this case are aileron  $\delta_a$ , elevator  $\delta_e$ , and rudder  $\delta_r$ . The coefficients  $C_{ij}$  with  $i = \{X, Y, Z, l, m, n\}$  and  $j = \{\alpha, \beta, p, q, r, \delta_a, \delta_e, \delta_r, 0\}$  are the *dimensionless aerodynamic derivatives* that need to be identified.

### 2.3 | Model assumptions and neglected dynamics

In flight dynamics, different methods of aerodynamic derivatives modeling exist. In many practical cases, the aerodynamic properties are approximated by linear terms in their Taylor series expansion as in (6). On the one hand, such approximations yield sufficient accuracy for attached flows.<sup>27</sup> On the other hand, this representation cannot be used in the region of  $\alpha$  where separated and vortex flow occurs.<sup>28</sup>

In this work, since the aircraft dynamics and its aerodynamic characteristics are described by the Equations (3), (4), (5), and (6), one has to implicitly account for the model mismatches summarized as follows.

- The aerodynamic model (5), (6) neglects the influence of parameter variation through time.<sup>26</sup> One can account for such a model mismatch either by introducing a first-order differential equation involving the angle of attack rate  $\dot{\alpha}$ <sup>28</sup> or by designing flight trajectories customized for energy production that allow the aircraft to perform mild maneuvers.<sup>20,21</sup>
- The mathematical model (3) relies on Euler's equations, which describe the motion of rigid bodies only, hence flexible modes are implicitly neglected. However, a rigid-wing aircraft for AWE is usually characterized by a high-strength wing with relatively high stiffness, as also expected for the next prototype shown in Figure 3. Eventual structural-coupling issues caused by flexible modes are addressed during the control architecture design.<sup>25</sup>
- The aerodynamic derivatives in (6) are implicitly a function of  $\alpha$ . Nevertheless, system identification performed via flight tests are typically valid only for small neighborhood of  $\alpha$  with respect to its trim value  $\alpha_e$  given at a specific trim airspeed  $V_{T_e}$ . Because aircraft deployed for AWES is intended to fly over a wide range of flight conditions, flight test maneuvers and parameter identification need to be performed at multiple trim conditions.
- Estimates of aerodynamic derivatives are computed assuming that the aircraft inertias are known a priori. However, fully accurate inertial estimates are difficult to obtain. Inertia estimates can be computed from computer-aided design models or swing tests with varying degrees of accuracy.<sup>29,30</sup> Errors in  $J_{\{x,y,z,xz\}}$  will lead to errors in the absolute estimates of the aerodynamic coefficients. Nevertheless, this will not undermine the predictive capability of the derived model, as long as the estimated derivatives are kept consistent with the assumed value of  $J_{\{x,y,z,xz\}}$  used to estimate them.<sup>5</sup>

In order to overcome the issues mentioned previously, it is a current practice to design a complex hierarchical control system with high margin of robustness and to fly patterns with specific boundary conditions (for further details, see the work of Ruiterkamp and Sieberling<sup>2</sup>).

## 3 | DESIGN AND EVALUATION OF INPUT SIGNALS

In this section, an insight into the flight operation procedure and the rationale behind is provided. Subsequently, conventional and optimized maneuvers are designed for parameter estimation purposes and assessed via the Cramer-Rao Lower Bound (CRLB).

### 3.1 | Flight test procedure for a high lift, autonomous aircraft

Typically, experiments are repeated on each axis to both obtain a rich data set and reduce the effect of sensor biases as well as colored noise (atmospheric turbulence) on the estimation results.<sup>5</sup> To prevent biases due to correlation between the measurement noise and the inputs, it is best to perform open-loop experiments.<sup>31</sup> For both physical and practical reasons, system identification flight tests are performed at *steady wing-level flight* condition.<sup>32</sup> An aircraft is in steady wing-level flight condition when its body angular rates ( $p, q, r$ ) and roll angle  $\phi$  are equal to zero and it flies with constant airspeed  $V_{T_e}$ .<sup>25</sup> Fulfillment of this steady condition allows decoupling of the aircraft motion in *longitudinal* and *lateral* dynamics, hence one can focus only on a subset of the entire aircraft dynamics, which is mainly excited from a given maneuver. For instance, if a signal excitation is performed along the longitudinal axis via elevator deflection (with propellers switched off), the remaining control surfaces (aileron and rudder deflection) are used to stabilize the lateral dynamics throughout the entire experiment. As a consequence, parameter estimation will be performed only on the excited dynamics, which is the longitudinal motion for this work. Note that, for the presented case study, the cross-product of inertia  $J_{xz}$  is only  $\approx 2\%$

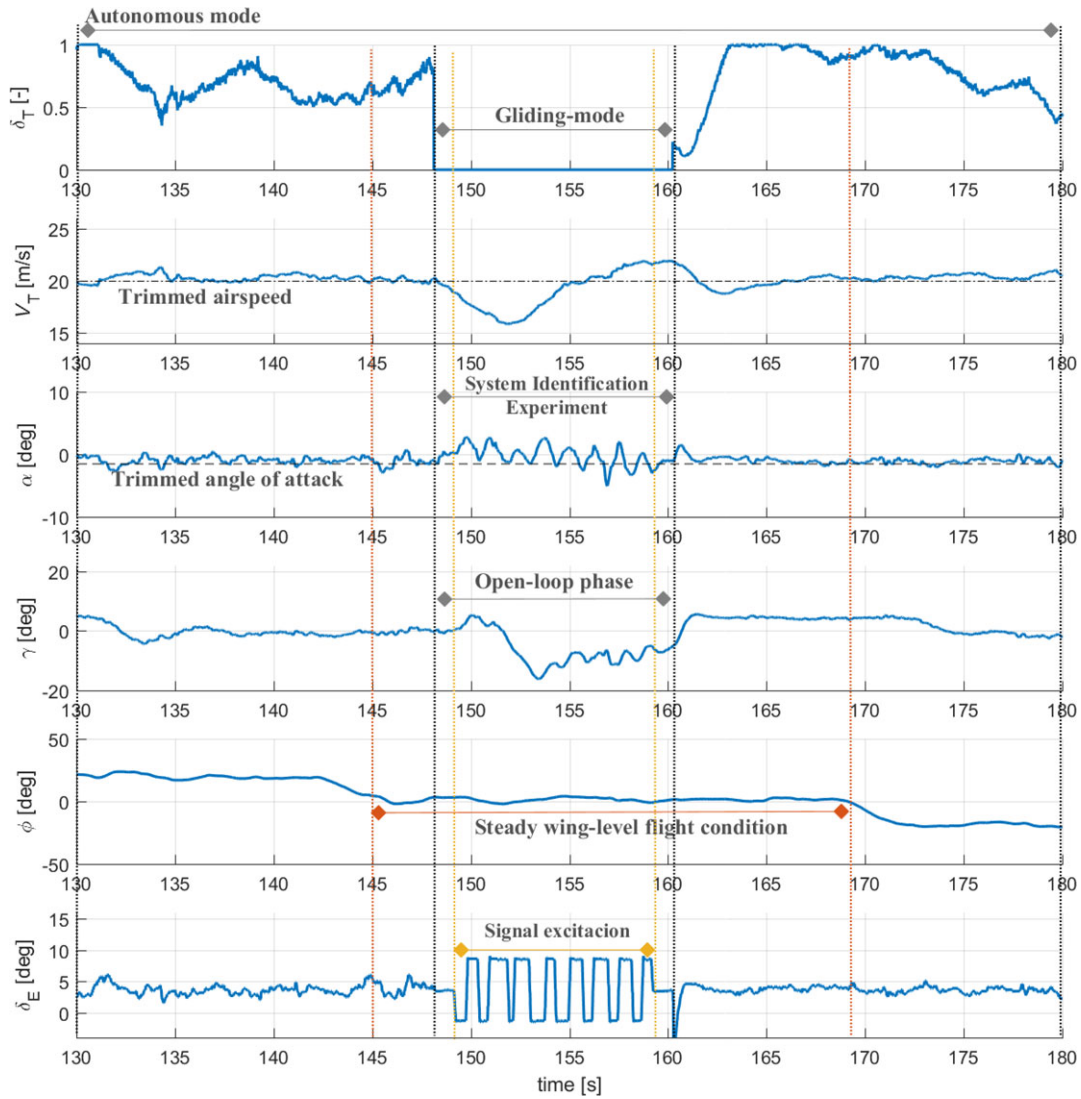


**FIGURE 5** Example of a flight test procedure for a high lift, autonomous aircraft (experimental data). After a coordinated turn,<sup>25</sup> the aircraft performs a straight flight ( $\phi \approx 0$  deg) with trimmed airspeed  $V_{T_e} \approx 20$  m/s and corresponding trimmed angle of attack  $\alpha_e \approx -2$  deg held by elevator deflection angle  $\delta_{e_e} \approx 3.5$  deg. The flight path angle  $\gamma$  is approximately zero prior to the gliding mode. Note that, for this case study, the propellers provide a pitch moment contribution since they are located on top of the fuselage, hence above the aircraft center gravity. Throughout the excitation of the longitudinal motion performed in gliding mode, the aircraft slightly descends as also shown by  $\gamma$ , although the angle of attack response remain within a neighborhood of  $\alpha_e$ . The data set is collected during the open-loop phase and despite a significant excitation of the longitudinal dynamics, the lateral motion is barely perturbed thanks to both the steady wing-level flight condition and the motion stabilization via aileron  $\delta_a$  and rudder  $\delta_r$  deflection. Subsequently, the propellers are switched on and the aircraft operates fully in closed-loop to recover via a steady regime, in this example a coordinated turn [Colour figure can be viewed at [wileyonlinelibrary.com](http://wileyonlinelibrary.com)]

w.r.t. the smallest moment of inertia, ie,  $J_x$ , hence minimal cross-coupling effects are expected, as also shown in (3) if one assumes  $J_{xz} = 0$ . Figure 5 depicts the flight test procedure described previously and adopted within this work.

### 3.2 | Decoupling of dynamics and aircraft modes

For conventional aircraft parameter estimation experiments, a linear perturbation model structure is usually taken into account.<sup>33</sup> Therefore, the flight test inputs are perturbations with respect to the steady condition. Within this work, data fitting is performed using the nonlinear formulation (3) relative to the longitudinal dynamics, though, linear representations are used for signal input design as well as assessment of the expected estimation performance. The longitudinal dynamics are described via LTI state-space form by the states  $\mathbf{x}_{lon} = [V_T \ \alpha \ \theta \ q]^T$ , which correspond to (3a), (3c), (3e),

and (3h). The forces  $X$ ,  $Z$ , and the moment  $M$  are assumed to be linear functions of  $V_T$ ,  $\alpha$ ,  $q$ , and the elevator deflection  $\delta_e$ , resulting in the following matrices:

$$\mathbf{A}_{\text{lon}} = \begin{bmatrix} X_V & X_\alpha & -g_D \cos \theta_e & X_q \\ Z_V & \frac{Z_\alpha}{V_{T_e}} & -g_D \sin \theta_e & Z_q \\ 0 & 0 & 0 & 1 \\ M_V & M_\alpha & 0 & M_q \end{bmatrix}, \quad \mathbf{B}_{\text{lon}} = \begin{bmatrix} X_{\delta_e} \\ \frac{Z_{\delta_e}}{V_{T_e}} \\ 0 \\ M_{\delta_e} \end{bmatrix}, \quad (7)$$

where the nonzero elements are known as *dimensional aerodynamic derivatives*, whereas  $\theta_e$  is the steady-state pitch angle. The dimensional derivatives can be converted into dimensionless derivatives as shown in (6) via the geometrical configuration of the aircraft (for details, see the works of Stevens et al<sup>25</sup> and Mulder et al<sup>26</sup>). The longitudinal dynamics can be further decoupled into the *phugoid* and *short-period* mode. The phugoid mode is normally rather slow, slightly dampened, and dominates the response in  $V_T$  and  $\theta$ , whereas the short-period mode is typically fast, moderately dampened, and dominates the response in  $\alpha$  and  $q$ . For control applications, accurate knowledge of the phugoid mode is not crucial due to the low frequency of oscillation, which is compensated via feedback control, whereas the short-period mode is crucial for stability and performance characteristics.<sup>34</sup>

The lateral dynamics are described analogously by the states  $\mathbf{x}_{\text{lat}} = [\beta \ \phi \ p \ r]^\top$ , which correspond to Equations 3b, (3d), (3g), and (3i). Force  $Y$  and moments  $L$  and  $N$  are described by linear functions of  $\beta$ ,  $p$ ,  $r$ , and inputs  $\mathbf{u}_{\text{lat}} = [\delta_a \ \delta_r]^\top$ . The resulting matrices are given by

$$\mathbf{A}_{\text{lat}} = \begin{bmatrix} \frac{Y_\beta}{V_{T_e}} & g_D \cos \theta_e & Y_p & Y_r - V_{T_e} \\ 0 & 0 & 1 & \tan \theta_e \\ L'_\beta & 0 & L'_p & L'_r \\ N'_\beta & 0 & N'_p & N'_r \end{bmatrix}, \quad \mathbf{B}_{\text{lat}} = \begin{bmatrix} \frac{Y_{\delta_a}}{V_{T_e}} & \frac{Y_{\delta_r}}{V_{T_e}} \\ 0 & 0 \\ L_{\delta_a}' & L_{\delta_r}' \\ N_{\delta_a}' & N_{\delta_r}' \end{bmatrix}, \quad (8)$$

and their derivatives are defined in the work of McRuer et al.<sup>35</sup> Unlike the longitudinal dynamics, the lateral motion cannot be decoupled into independent modes. They are governed by a slow *spiral* mode, a fast lightly damped *Dutch roll* mode, and an even faster *roll subsidence* mode (for details, see the work of Stevens et al<sup>25</sup>).

### 3.3 | Design of conventional maneuvers

A type of signal input for this application, which is widely used in the aerospace field due to its easy implementation and good estimation performance, comes from an optimization procedure of a sequence of step functions developed by Koehler and Wilhelm.<sup>36</sup> The input signal has a bang-bang behavior with a duration  $7\Delta T$  with switching times at  $t = 3\Delta T$ ,  $t = 5\Delta T$ , and  $t = 6\Delta T$  and amplitude  $A$ . For this reason, such an input signal is called a *3-2-1-1 maneuver*.

In the work of Mulder et al,<sup>37</sup> it was shown that the 3-2-1-1 maneuver provides the best estimation accuracy for both aircraft longitudinal and lateral dynamics among *Doublets*, *Mehra*, *Schulz*, and *DUT* input signals. Thus, only Doublets and 3-2-1-1 input signals provide sufficient system excitation for identification of system responses with frequencies above 1 Hz, although the 3-2-1-1 maneuver embraces much higher frequencies compared to Doublets. Finally, 3-2-1-1 maneuvers can be chosen through both a qualitative consideration in the frequency domain<sup>38</sup> and a *trial-and-error* approach in order to ensure that the system response is within the flight envelope.

### 3.4 | Design of optimized maneuvers

Another type of signal input implemented within this work is obtained by solving a time-domain model-based OED problem that aims to obtain more accurate parameter estimates while enforcing safety constraints.<sup>18</sup>

The main idea of OED is to use, as an objective of an optimization problem, a function  $\Psi(\cdot)$  of the Fisher information matrix  $\mathbf{F}$ , which is given by

$$\mathbf{F} = \sum_{i=1}^N \left[ \left( \frac{\partial \mathbf{y}(i)}{\partial \mathbf{p}} \right)^\top \boldsymbol{\Sigma}_y^{-1} \left( \frac{\partial \mathbf{y}(i)}{\partial \mathbf{p}} \right) \right], \quad (9)$$

with  $\mathbf{y} \in \mathbb{R}^{n_y}$  being the output states sampled in  $N$  measurements and a priori parameters  $\mathbf{p} \in \mathbb{R}^{n_p}$  and  $\boldsymbol{\Sigma}_y \in \mathbb{R}^{n_y \times n_y}$  being the measurements for noise covariance matrix. A general model-based OED problem, which considers input  $\mathbf{u}(t)$ ,

differential states  $\mathbf{x}(t)$ , time length  $T$ , and subject to a mathematical model expressed as an ODE can be formulated as

$$\underset{\mathbf{x}(\cdot), \mathbf{u}(\cdot)}{\text{minimize}} \quad \Psi(\mathbf{F}[\mathbf{x}(\cdot), \mathbf{u}(\cdot), \tilde{\mathbf{p}}]) \quad (10a)$$

$$\text{subject to:} \quad \dot{\mathbf{x}}(t) = \mathbf{f}(\mathbf{x}(t), \mathbf{u}(t), \tilde{\mathbf{p}}), t \in [0, T] \quad (10b)$$

$$\mathbf{x}(0) = \mathbf{x}_0, \quad (10c)$$

$$\mathbf{u}_{\min} \leq \mathbf{u}(t) \leq \mathbf{u}_{\max}, t \in [0, T] \quad (10d)$$

$$\mathbf{x}_{\min} \leq \mathbf{x}(t) \leq \mathbf{x}_{\max}, t \in [0, T]. \quad (10e)$$

For further details, see the works of Licitra et al<sup>19</sup> and Ampyx Power B.V.<sup>39</sup>

### 3.5 | Baseline model

Both 3-2-1-1 and OED-based maneuvers need to be designed using a baseline (a priori) model with reasonable accuracy in order to both have a first insight about the estimation performance and ensure that the system response evolves within the flight envelope.

Various methods can be applied to obtain a first approximation of the aerodynamic model with the corresponding prior parameters  $\tilde{\mathbf{p}}$ . If the airframe is similar to an existing aircraft, its model can be scaled. For instance, the digital DATCOM<sup>15</sup> is a purely empirical guide to estimate aerodynamic derivatives based on aircraft configuration and the experience of engineers. If the airfoils and aircraft configurations are new, one can perform analysis via the lifting line method,<sup>40</sup> CFD,<sup>14</sup> wind-tunnel tests, or previous flight tests. Depending on the available resources, combinations of these methods can be used. In this work, a priori models are retrieved from lifting line method.<sup>5</sup>

A steady wing-level flight condition is considered with trimmed airspeed  $V_{T_e} = 20$  m/s. Subsequently, the system is linearized and the longitudinal dynamics are taken into account as in (7) with dimensional a priori derivatives shown in Table A2.

As mentioned in Section 3.1, the a priori models provide an insight into the general characteristics of the aircraft behavior via modal analysis.<sup>25</sup> In Table 1, the a priori aircraft modes relative to the longitudinal dynamics are provided in terms of natural frequencies  $\omega_n$ , damping ratios  $\delta$ , time constant(s)  $\tau$ , overshoots in percentage  $S_{\%}$ , and period of oscillations  $P_O$ , whereas Figure 6 shows the candidate maneuvers with the corresponding simulation model response.

The modal analysis suggests to design experiments with time duration longer than 12.067 seconds in order to provide sufficient excitation in the frequency range where the expected phugoid mode should take place. Although, the optimized experiments' length is set to 10 seconds to ensure that the full sequence is completed in the available flight test area, taking into account variations in the wind conditions on the flight test day(s) (for further details, see the works of Licitra et al<sup>18,19</sup>).

Historically, aircraft system identification has been performed using a pilot to provide input sequences. In this work, the input sequences are performed autonomously. The flight control computer monitors the aircraft response and aborts the maneuver in case the predetermined flight envelope boundaries are violated.<sup>5,18,19</sup>

### 3.6 | Preliminary analysis

One way to assess the estimation accuracy that a given maneuver can provide is by the CRLB, ie, the theoretical lower limits for parameter standard errors  $\sigma$  using an efficient and asymptotically unbiased estimator, such as maximum likelihood.<sup>41</sup> A performance analysis of signal inputs computed via the CRLB isolates the merits of the input design from

**TABLE 1** A priori longitudinal modes

| Mode       | Short-period | Phugoid | Unit  |
|------------|--------------|---------|-------|
| $\omega_n$ | 3.939        | 0.521   | rad/s |
| $\tau$     | 0.254        | 1.920   | s     |
| $\delta$   | 0.789        | 0.031   | –     |
| $S_{\%}$   | 1.768        | 90.831  | %     |
| $P_O$      | 2.596        | 12.067  | s     |

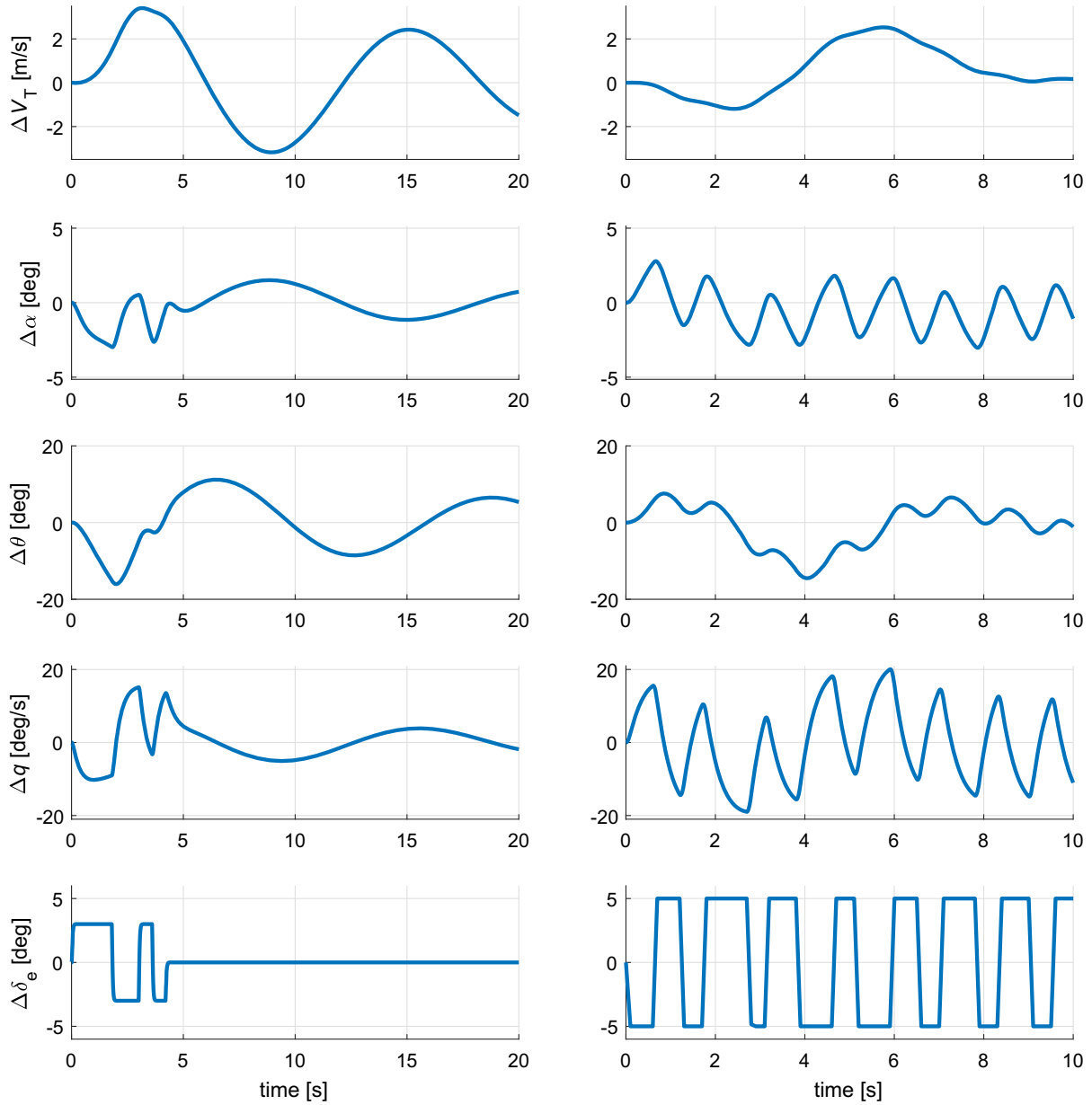


**FIGURE 6** Simulation model response using both 3-2-1-1 (left) and optimized maneuvers (right) and shown as perturbations with respect to the trim condition [Colour figure can be viewed at [wileyonlinelibrary.com](http://wileyonlinelibrary.com)]

the merits of the parameter estimation algorithm used to extract the aerodynamic derivatives from the flight data.<sup>33</sup> The CRLB depends on the diagonal entries of the Fisher information matrix  $\mathbf{F}$  (9), which is formally<sup>31</sup>

$$\sigma_i \geq \text{CRLB}_i = \frac{1}{\sqrt{\mathbf{F}_{ii}}}. \quad (11)$$

Experience has shown that a factor of 2 can be introduced in order to obtain an approximation of the parameter standard error,<sup>42</sup> resulting in

$$\sigma_i \approx 2 \cdot \text{CRLB}_i = \frac{2}{\sqrt{\mathbf{F}_{ii}}}. \quad (12)$$

Finally, note that the inverse of the Fisher information matrix  $\mathbf{F}^{-1}$  corresponds to the covariance matrix of the estimated parameters  $\Sigma_{\mathbf{p}} \in \mathbb{R}^{n_p \times n_p}$ . Table 2 gathers the 2CRLB values in percentage for the system responses shown in Figure 6 and uses the sensors' noise standard deviation  $\sigma_y$  collected in Table A3.

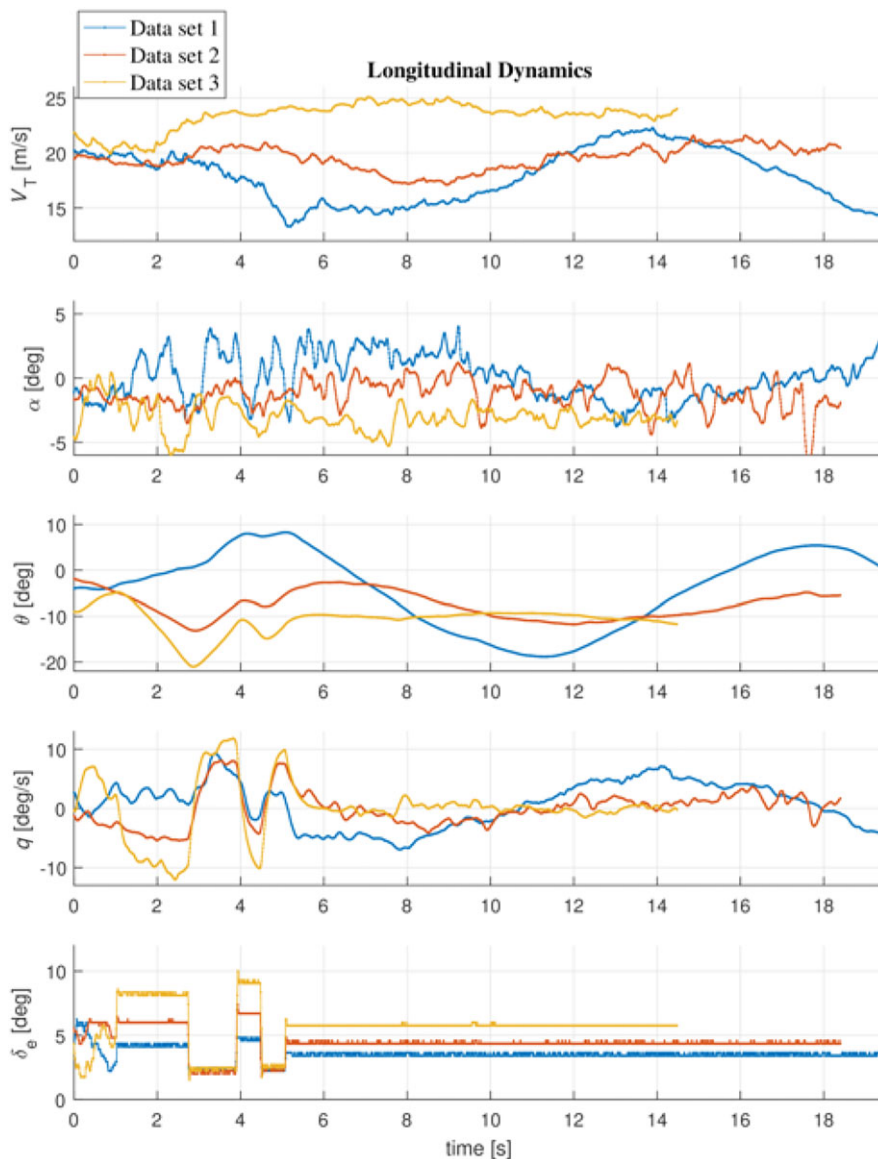
The results indicate that the dimensional aerodynamic derivatives relative to the phugoid mode, ie,  $X_q$ ,  $X_{\delta_e}$ , which correspond to the dimensionless one  $C_{X_q}$ ,  $C_{X_{\delta_e}}$  are subject to high uncertainty. High values of CRLB indicate that either the

**TABLE 2** Dimensional aerodynamic longitudinal derivatives with corresponding expected estimation accuracy via 2CRLB

|                          | $X_V$ | $X_\alpha$ | $X_q$  | $X_{\delta_e}$ | $Z_V$ | $Z_\alpha/V_{T_c}$ | $Z_q$ | $Z_{\delta_e}/V_{T_c}$ | $M_\alpha$ | $M_q$ | $M_{\delta_e}$ |
|--------------------------|-------|------------|--------|----------------|-------|--------------------|-------|------------------------|------------|-------|----------------|
| <b>Value</b>             | -0.06 | 8.63       | -0.153 | -0.17          | -0.05 | -4.22              | 0.90  | -0.34                  | -7.67      | -1.96 | -17.94         |
| <b>2CRLB<sub>%</sub></b> | 25.27 | 34.88      | 336.67 | 291.62         | 1.07  | 1.06               | 1.08  | 4.18                   | 0.14       | 0.10  | 0.02           |

$i$ th parameter is physically insignificant with respect to the measured aircraft response or there is a correlation between parameters, ie, these parameters can vary together, making their individual values difficult to determine.<sup>31</sup> In this case, the contribution provided to the aircraft response by  $X_V$  is quite negligible; additionally, a significant correlation occurs between  $X_\alpha$ ,  $X_q$ , and  $X_{\delta_e}$ .

To overcome this issue, one might fix the parameters associated to the phugoid mode with their a priori values, although errors in the form of a low-frequency model mismatch could arise in the identified model. Nevertheless, accurate knowledge of the phugoid mode is not crucial due to its slow motion, which can be easily handled by a pilot or a control system.<sup>32</sup> On the other hand, high estimation accuracy is required for the short-period mode, which is given by  $Z_V$ ,  $Z_\alpha$ ,  $Z_q$ ,  $Z_{\delta_e}$ ,

**FIGURE 7** Three experimental data sets obtained through conventional maneuvers ( $V_{T_c} = 20\text{ m/s}$ ). Average wind speed  $\approx 7\text{ m/s}$  [Colour figure can be viewed at [wileyonlinelibrary.com](http://wileyonlinelibrary.com)]

$M_\alpha$ ,  $M_q$ , and  $M_{\delta_e}$  since longitudinal stability and performance characteristics primarily depend on the accuracy of the short-period mode.<sup>34</sup>

#### 4 | EXPERIMENTAL DATA

A total of six experimental data sets are collected within two independent flight test campaigns with trimmed airspeed  $V_{T_e} = 20\text{ m/s}$ . Three experiments are performed with conventional maneuvers 3-2-1-1 shown in Figure 7 with an average (estimated) wind speed  $\approx 7\text{ m/s}$ , whereas the other three experiments are collected using the OED-based maneuvers and shown in Figure 8 with average wind speed  $\approx 2\text{ m/s}$ .

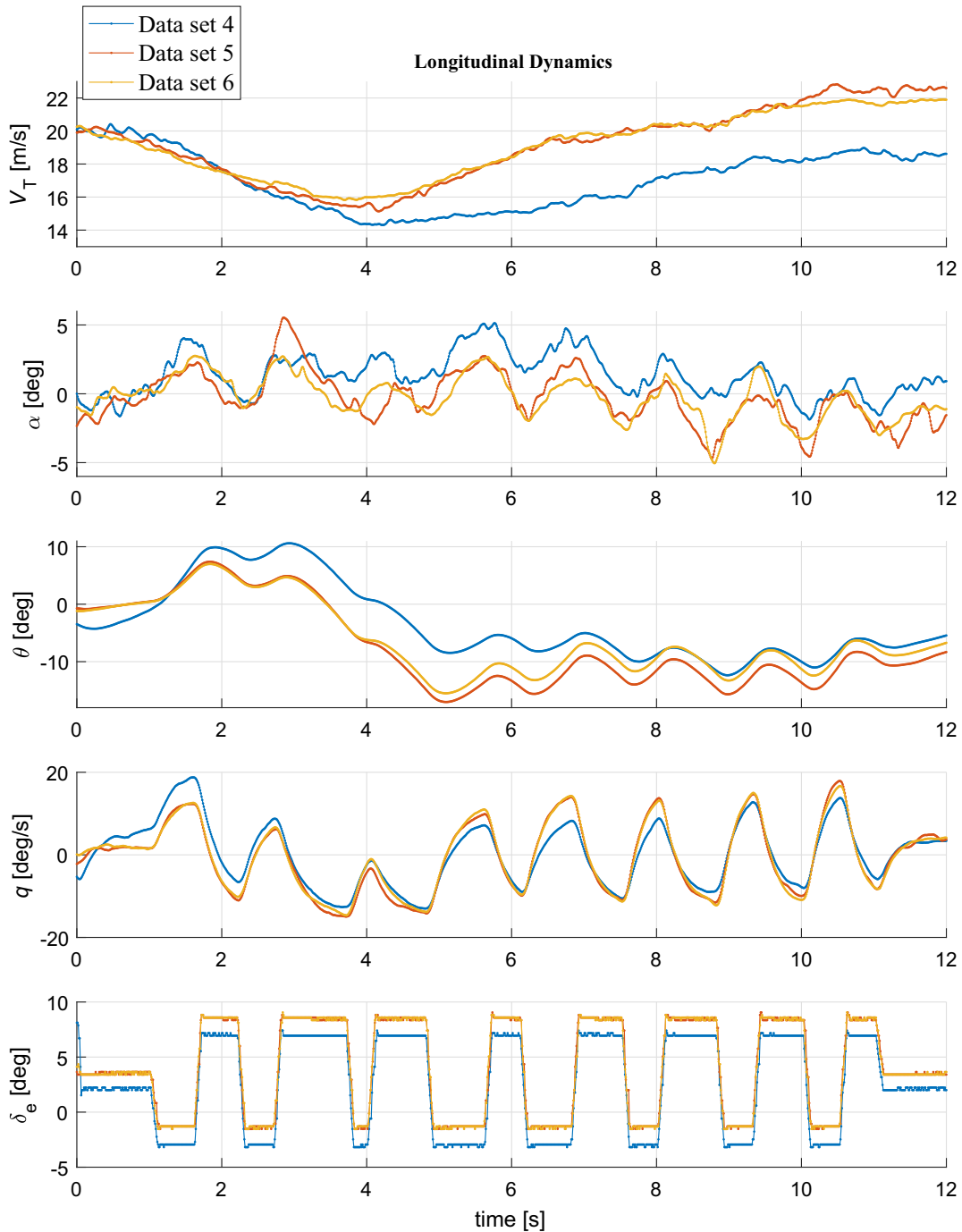


**FIGURE 8** Three experimental data sets obtained through optimized maneuvers ( $V_{T_e} = 20\text{ m/s}$ ). Average wind speed  $\approx 2\text{ m/s}$  [Colour figure can be viewed at [wileyonlinelibrary.com](http://wileyonlinelibrary.com)]

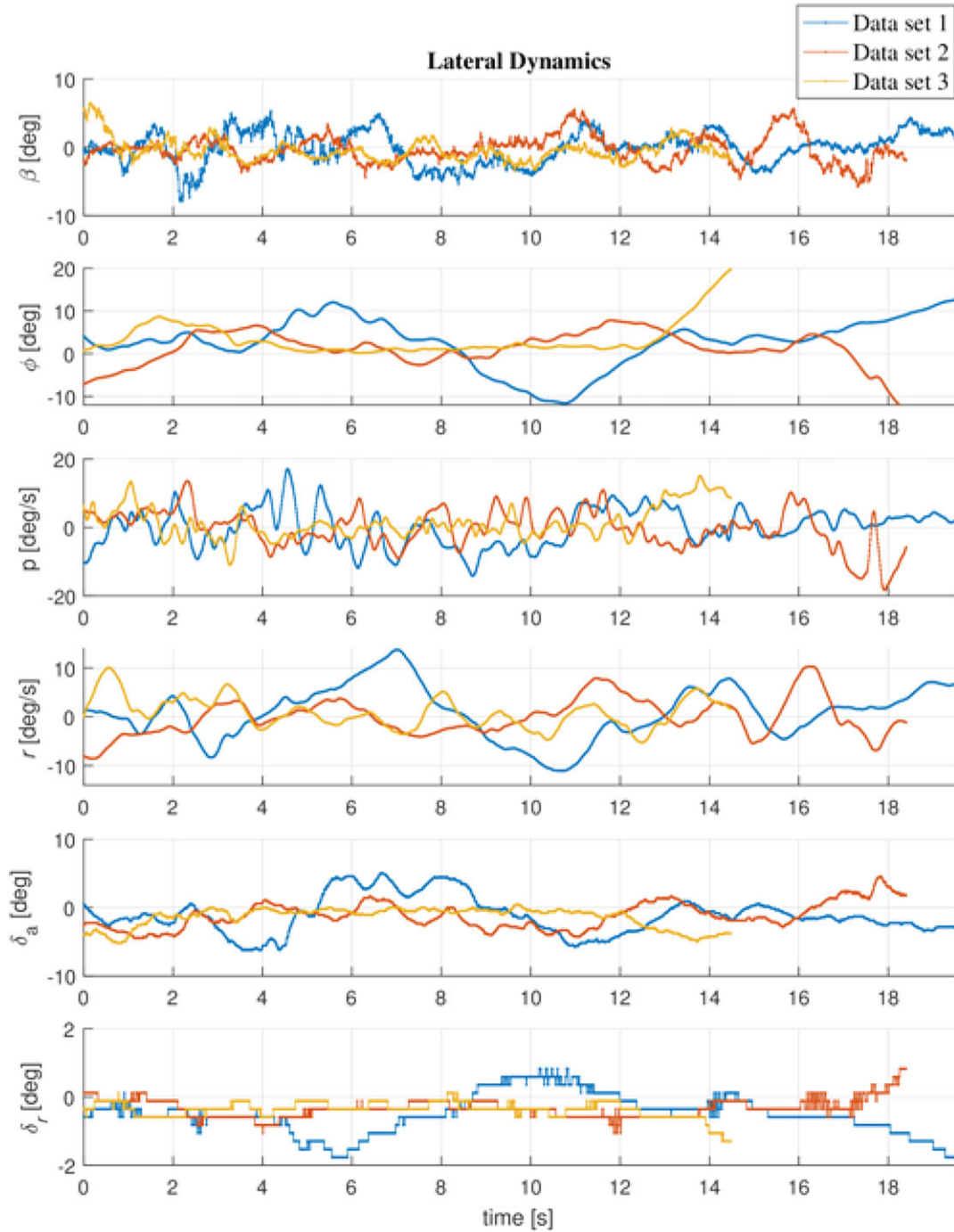


**FIGURE 9** Stabilization of lateral dynamics by  $\delta_a$  and  $\delta_r$  during excitation signal along the longitudinal dynamics via conventional maneuvers ( $V_T = 20\text{m/s}$ ). Average wind speed  $\approx 7\text{m/s}$  [Colour figure can be viewed at [wileyonlinelibrary.com](https://onlinelibrary.wiley.com)]

In Figure 8, one can observe the decoupling between the phugoid mode, which dominates the airspeed  $V_T$  and pitch  $\theta$  responses, and the fast changes on the angle of attack  $\alpha$  and pitch rate  $q$  coming from the short-period mode. Comparing Figure 7 with Figure 8, it is possible to discern the turbulence effect on the angle of attack  $\alpha$  and pitch rate  $q$  response. This is not surprising since turbulences increase consistently with the wind speed.

As mentioned in Section 3.1, during the excitation of the longitudinal dynamics, the lateral motion is stabilized by aileron  $\delta_a$  and rudder  $\delta_r$  deflection. Figures 9 and 10 show the lateral dynamics relative to the conventional and optimized experiments, respectively. In addition, in this case, it is clearly shown how the turbulence effect acts on the aircraft dynamics.

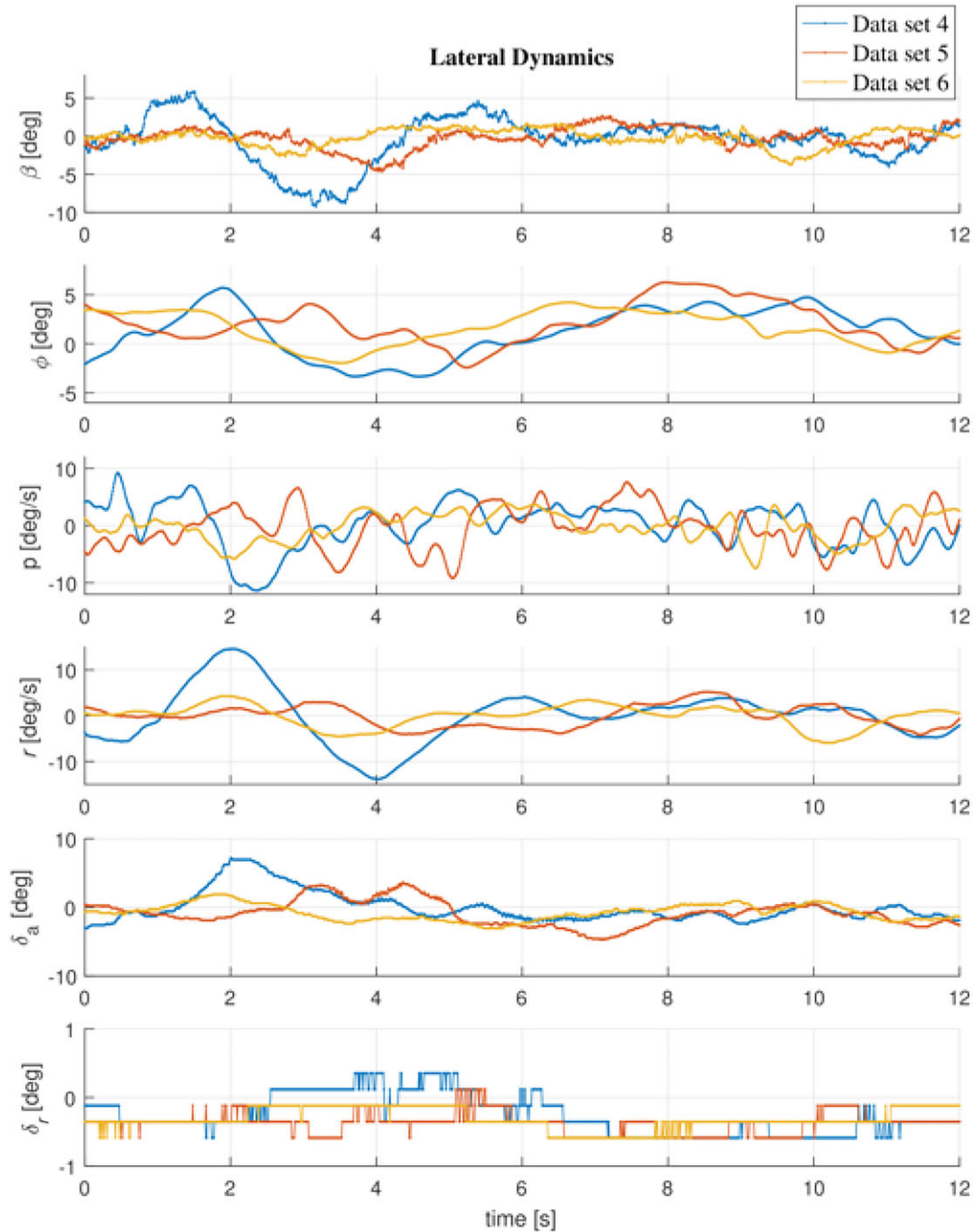


**FIGURE 10** Stabilization of lateral dynamics by  $\delta_a$  and  $\delta_r$  during excitation signal along the longitudinal dynamics via optimized maneuvers ( $V_{T_c} = 20\text{ m/s}$ ). Average wind speed  $\approx 2\text{ m/s}$  [Colour figure can be viewed at [wileyonlinelibrary.com](http://wileyonlinelibrary.com)]

More precisely, in Figure 9, one can observe how the roll rate  $p$  and roll angle  $\phi$  appear sensitive to the turbulence, which involves a major control effort from the aileron deflection  $\delta_a$  in order to both stabilize this axis and prevent flight envelope violation.

## 5 | FORMULATION OF MULTIPLE-EXPERIMENT MODEL-BASED PARAMETER ESTIMATION

Whenever parameter estimation is intended for identification of aircraft dynamics, multiple experiments are usually required to deal with the following issues.<sup>43</sup>

- Multiple experiments reduce the effects of sensor biases as well as atmospheric turbulence on estimation results.
- Individual maneuvers usually have good information content only for a subset of parameters, while multiple maneuvers combined can provide better information w.r.t the complete set of parameters.
- The flight test area and operating safety case restrict the flight paths that can be flown, limiting the available duration of any particular maneuver.

A standard approach is to retrieve the estimated parameters via data fitting for each independent experiment and subsequently weight them w.r.t. their inverse (estimated) parameter covariance matrix  $\Sigma_{\mathbf{p}}$ .<sup>44</sup> However, such method might lead to wrong results whenever computed values of  $\Sigma_{\mathbf{p}}$  are not reliable.<sup>5</sup>

Furthermore, as shown in Equation (3), the angular acceleration measurements ( $\dot{p}, \dot{q}, \dot{r}$ ) as well as rate of changes in the airspeed  $V_T$ , Euler ( $\phi, \theta, \psi$ ), and aerodynamic angles ( $\alpha, \beta$ ) need to be available in order to estimate aerodynamic properties. Usually, these quantities are not measured, although they can be retrieved by numerical differentiation methods, which are rather noisy.<sup>43</sup> Consequently, signal distortion may arise, degrading the overall estimation performance. Within this scenario, multiple experiments MBPE algorithms appear a reasonable choice for estimation of aerodynamic derivatives.

In this context, let us consider a mathematical model defined as a set of ODE

$$\dot{\mathbf{x}}(t) = \mathbf{f}(\mathbf{x}(t), \mathbf{u}(t), \mathbf{p}, t) \quad (13a)$$

$$\mathbf{y}(t) = \mathbf{h}(\mathbf{x}(t), \mathbf{u}(t), \mathbf{p}, t) + \boldsymbol{\epsilon}(t) \quad (13b)$$

with differential states  $\mathbf{x} \in \mathbb{R}^{n_x}$ , output state  $\mathbf{y} \in \mathbb{R}^{n_y}$ , noise-free control inputs  $\mathbf{u} \in \mathbb{R}^{n_u}$ , parameters  $\mathbf{p} \in \mathbb{R}^{n_p}$ , and time  $t$ . The measurement values  $\mathbf{y}$  are polluted by additive, zero-mean Gaussian noise  $\boldsymbol{\eta}(0, \Sigma_{\mathbf{y}})$  with  $\Sigma_{\mathbf{y}}$  the covariance matrix of measurements noise.

A multiple experiments MBPE problem can be first stated using an optimal control problem (OCP) perspective in continuous time as follows<sup>5</sup>:

$$\underset{\mathbf{p}(\cdot)}{\text{minimize}} \quad \sum_{i=1}^{N_e} \int_0^{T^i} \left\| \hat{\mathbf{y}}^i(t) - \mathbf{h}(\mathbf{x}^i(t), \hat{\mathbf{u}}^i(t), \mathbf{p}) \right\|_{\Sigma_{\mathbf{y}}^{-1}}^2 dt \quad (14a)$$

$$\text{subject to} \quad \dot{\mathbf{x}}^i(t) = \mathbf{f}(\mathbf{x}^i(t), \hat{\mathbf{u}}^i(t), \mathbf{p}, t) \quad (14b)$$

$$t \in [0, T^i], \quad i \in \mathbb{Z}_1^{N_e} \quad (14c)$$

with  $N_e$  being the number of experiments and  $\hat{\mathbf{u}}^i(t)$  and  $\hat{\mathbf{y}}^i(t)$  being the input and output measurements, respectively, for the  $i$ th experiment running for a duration  $T^i$ . Using *direct methods*,<sup>45</sup> the optimization problem (14) can be transformed into a finite dimensional nonlinear program (NLP), which can then be solved by numerical optimization methods. In this work, a *direct multiple shooting* approach is chosen due to its stability w.r.t. the initial guess compared to a *single shooting* strategy.<sup>46</sup>

In order to implement a multiple shooting algorithm, let us define an equidistant grid over the experiment consisting of the collection of time points  $t_k$ , where  $t_{k+1} - t_k = \frac{T^i}{N_m^i} := T_s, \forall i = 0, \dots, N_e$  with  $N_m^i$  the number of measurements for the  $i$ th data set, assuming implicitly that the measurements are collected with a fixed sample time  $T_s$ . Additionally, we consider a piecewise constant control parametrization  $\mathbf{u}(\tau) = \mathbf{u}_k$  for  $\tau \in [t_k, t_{k+1})$ . A function  $\mathbf{\Pi}(\cdot)$  over each shooting interval is given, which represents a numerical approximation for the solution  $x_{k+1}$  of the following initial value problem:

$$\dot{\mathbf{x}}(\tau) = \mathbf{f}(\mathbf{x}(\tau), \mathbf{u}_k, \mathbf{p}, \tau), \quad \tau \in [t_k, t_{k+1}]. \quad (15)$$

Within this work, for  $\mathbf{\Pi}(\cdot)$ , a Runge-Kutta integrator of order 4 (RK4) is implemented. Therefore, the OCP (14) can be translated into the NLP

$$\underset{\mathbf{p}, \mathbf{X}}{\text{minimize}} \quad \sum_{i=1}^{N_e} \sum_{k=0}^{N_m^i} \left\| \hat{\mathbf{y}}_k^i - \mathbf{h}(\mathbf{x}_k^i, \hat{\mathbf{u}}_k^i, \mathbf{p}) \right\|_{\Sigma_{\mathbf{y}}^{-1}}^2 \quad (16a)$$

$$\text{subject to} \quad \mathbf{x}_{k+1}^i - \mathbf{\Pi}(\mathbf{x}_k^i, \hat{\mathbf{u}}_k^i, \mathbf{p}) = 0 \quad (16b)$$

$$k = 0, 1, \dots, N_m^i - 1, \quad i \in \mathbb{Z}_1^{N_e}, \quad (16c)$$

where  $\mathbf{X} \in \mathbb{R}^{n_x}$  with  $n_x = \sum_{i=1}^{N_e} n_x \cdot N_m^i$  and sorted as

$$\mathbf{X} = \left[ x_0^1, \dots, x_{N_m^1-1}^1, \dots, x_0^{N_e}, \dots, x_{N_m^{N_e}-1}^{N_e} \right]^T \quad (17)$$

in order to create a block diagonal structure on the NLP formulation and especially in the equality constraints (16b). Notice that, in (17) the number of measurements  $N_m$  are assumed different for each  $i$ th experiment.

Finally, the NLP initialization can be chosen from, eg, previous estimates of  $\mathbf{p}$ , whereas  $\mathbf{X}$  can be initialized using the measurements  $\hat{\mathbf{y}}$  and/or estimates of the state  $\mathbf{x}$ . For further details, see the works of Diehl<sup>45</sup> and Bock et al.<sup>47</sup>

## 6 | PARAMETER ESTIMATION RESULTS

In this section, the parameter estimation (PE) is carried out on the experimentally obtained data. The estimation results are subsequently assessed via a time-domain model validation approach.

### 6.1 | Data fitting

Within this work, the MBPE algorithm is implemented using CASADI<sup>48</sup> in MATLAB environment. The system dynamics (13a) taken into account are the nonlinear longitudinal motions expressed in (3a), (3c), (3e), (3h) with differential states

$$\mathbf{x}(t) = [V_T(t) \alpha(t) \theta(t) q(t)]^T, \quad (18)$$

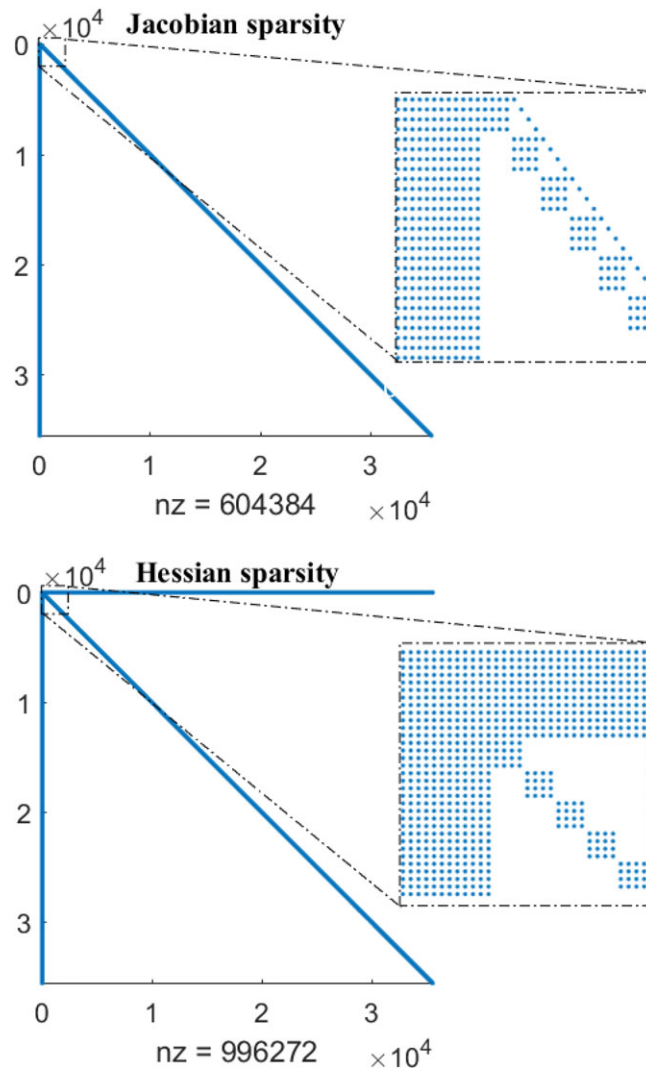


**FIGURE 11** Jacobian and Hessian Sparsity of the nonlinear program [Colour figure can be viewed at wileyonlinelibrary.com]

assuming steady wing-level flight condition, ie,  $\beta = \phi = p = r = 0$ . The unknown parameters are

$$\mathbf{p} = \left[ C_{X_0} \ C_{X_\alpha} \ C_{X_q} \ C_{X_{\dot{\delta}_e}} \ C_{Z_0} \ C_{Z_\alpha} \ C_{Z_q} \ C_{Z_{\dot{\delta}_e}} \ C_{m_0} \ C_{m_\alpha} \ C_{m_q} \ C_{m_{\dot{\delta}_e}} \right] \in \mathbb{R}^{12} \quad (19)$$

and control input equal to

$$\mathbf{u}(t) = \delta_e(t), \quad (20)$$

whereas the output states (13b) are simply given by

$$\mathbf{y}(t) = \mathbf{x}(t) + \boldsymbol{\epsilon}(t). \quad (21)$$

The continuous-time optimization problem (14) is subsequently discretized and formulated as an NLP using direct multiple shooting. The resulting NLP is solved via IPOPT<sup>49</sup> with linear solver MA27.<sup>50</sup> Finally, the optimization problem (16) is initialized using the baseline model described in Section 3.5 for  $\mathbf{p}$  and  $\mathbf{X}$  with the real output measurements  $\hat{\mathbf{y}}^i, i \in \mathbb{Z}_1^{N_e}$ .

Data fitting is carried out simultaneously for all experimental data set shown in Section 4 with total number of optimization variables

$$n_{\text{opt}} = n_{\mathbf{p}} + n_{\mathbf{X}} = 12 + 35564 = 35576. \quad (22)$$

The CASADI discovers the structure and computes the full sparse Jacobian and Hessian with a minimum of algorithmic differentiation sweeps (see Figure 11). The CASADI'S for-loop equivalents are used to efficiently build up the large number

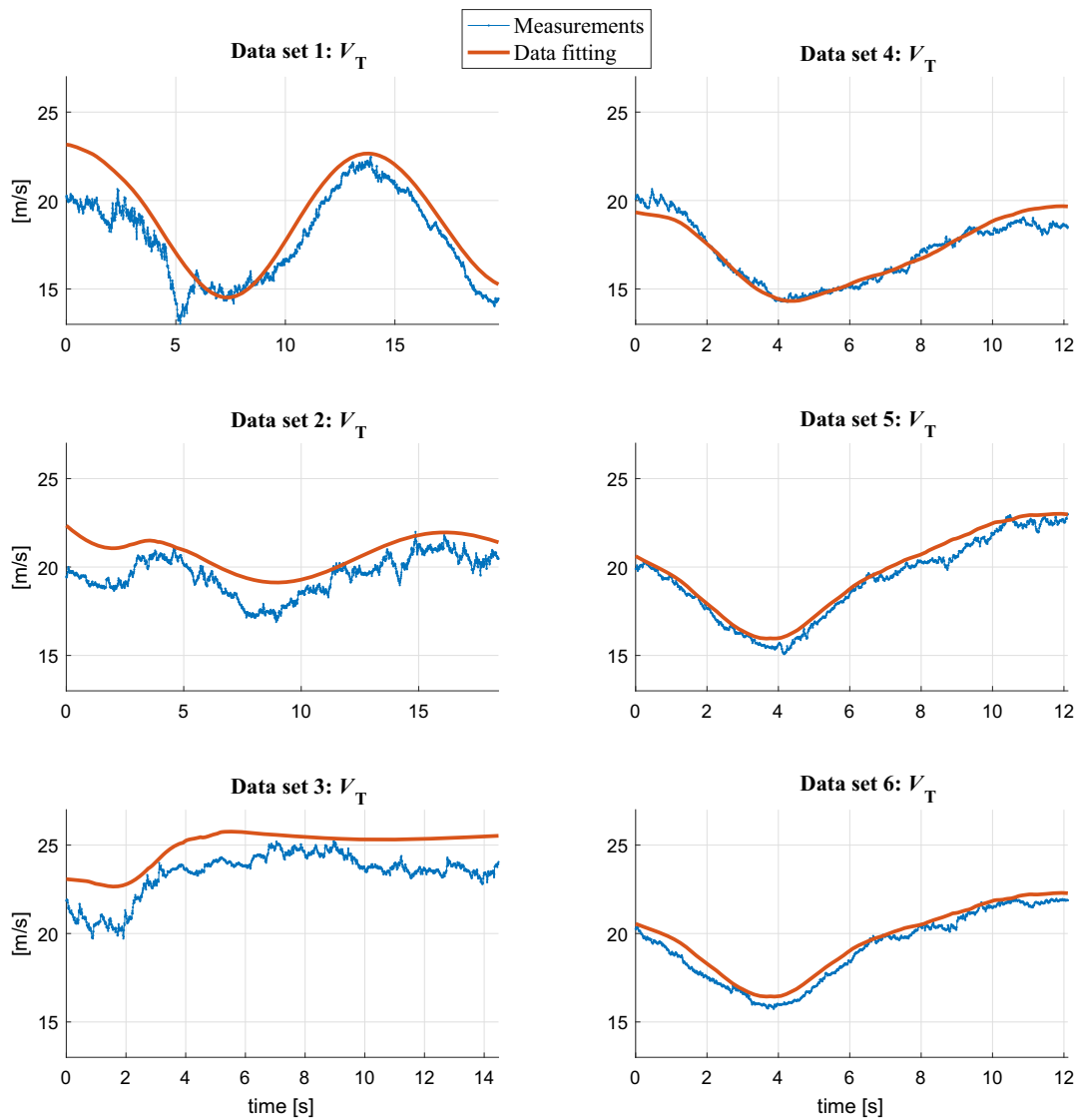


**FIGURE 12** Data fitting for multiple experiments along the longitudinal dynamics for  $V_{T_c} = 20\text{m/s}$ : airspeed  $V_T$  [Colour figure can be viewed at [wileyonlinelibrary.com](http://wileyonlinelibrary.com)]

of shooting constraints (16b). Furthermore, since this application requires a large number of control intervals, the CASADI map functionality was used to achieve a memory-lean computational graph. Using this proposed implementation, the NLP is solved within 28 iterations of IPOPT. Figures 12, 13, 14, and 15 show the data fitting for the airspeed  $V_T$ , angle of attack  $\alpha$ , pitch angle  $\theta$ , and pitch rate  $q$ , respectively, corresponding to the experimental data shown in Section 4. Note that the measurements are suitably low-pass filtered using zero-lag filtering in order to focus on the rigid-body modes only. The control surface inputs are measured via feedback sensors on the aircraft, which allows the estimation to proceed without requiring knowledge of the actuator dynamics. The control surface deflection measurements have no discernible noise, although quantization errors equal to 0.25 deg are presented and compensated. Furthermore, a one frame transport delay of the measurements is used.

The overall data fitting is satisfactory except for the airspeed  $V_T$ , where biases arise mainly in the conventional experiments. Finally, Table 3 collects the estimated dimensionless aerodynamic longitudinal derivatives for different trimmed airspeeds  $V_{T_e}$ . In particular, the remaining derivatives are carried out using five experimental data sets for each flight condition and using the same methodology described within this work, although the latter are not shown for the sake of brevity.

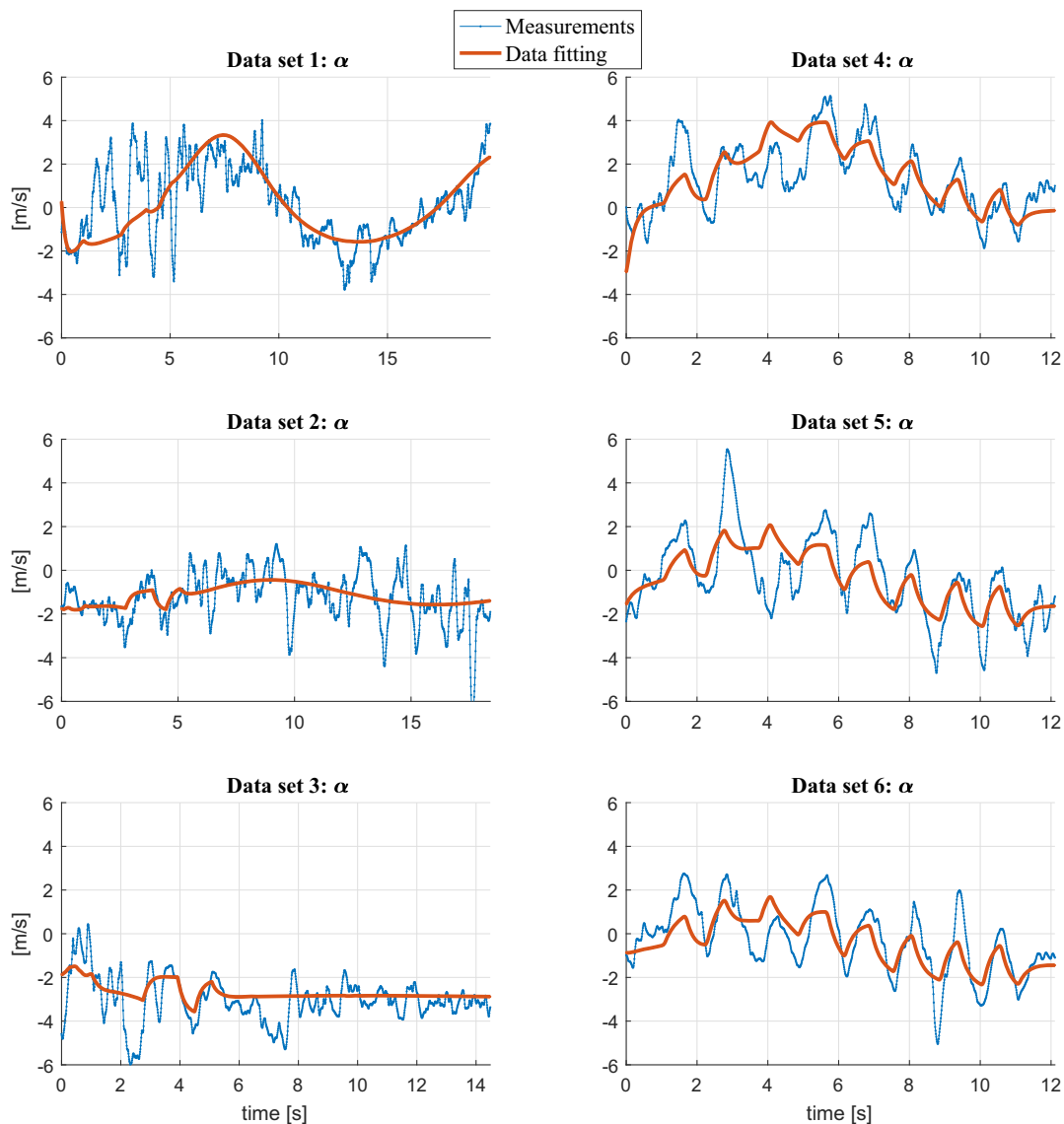


**FIGURE 13** Data fitting for multiple experiments along the longitudinal dynamics for  $V_{T_e} = 20\text{m/s}$ : angle of attack  $\alpha$  [Colour figure can be viewed at [wileyonlinelibrary.com](http://wileyonlinelibrary.com)]

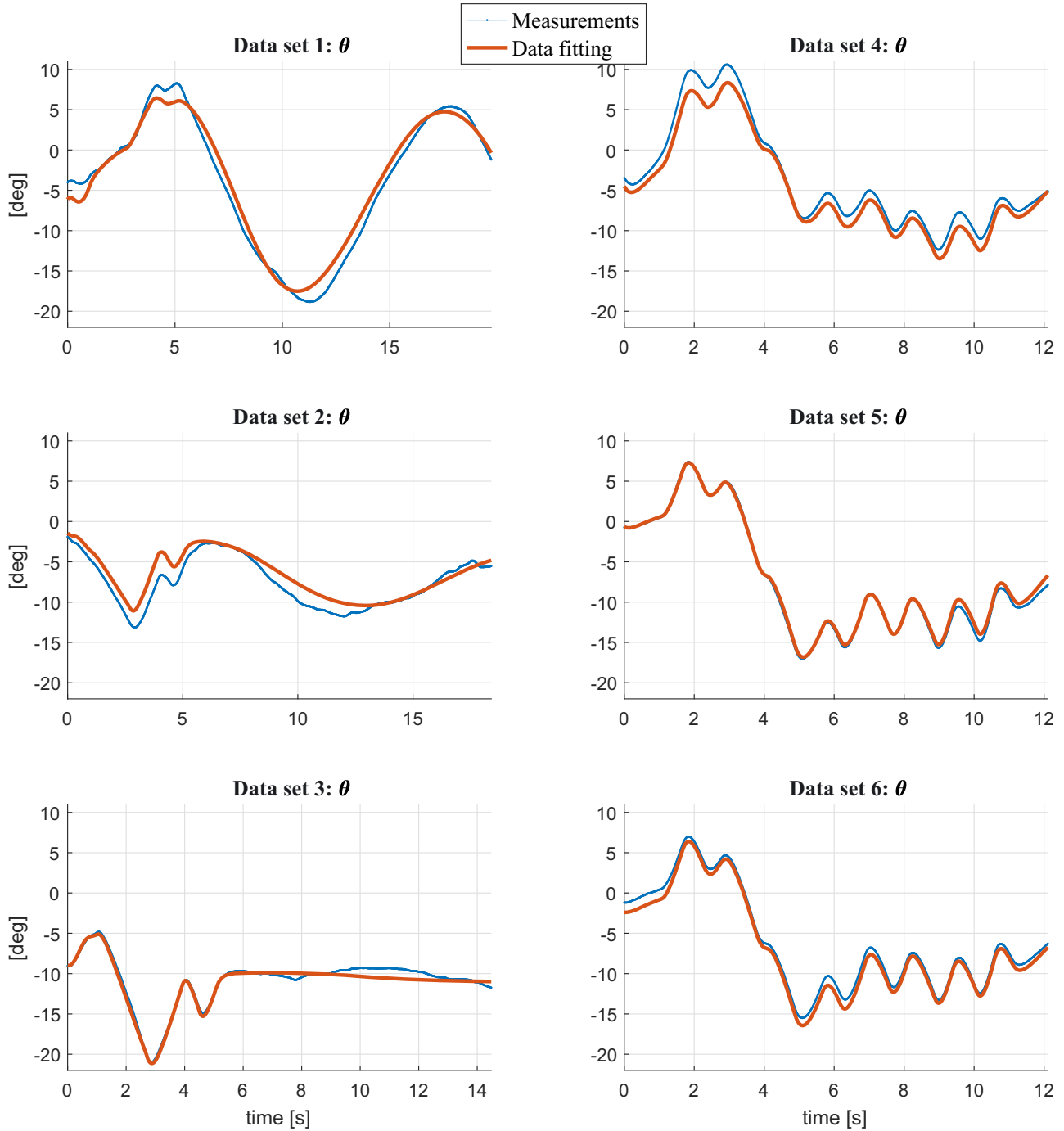


**FIGURE 14** Data fitting for multiple experiments along the longitudinal dynamics for  $V_{T_e} = 20\text{m/s}$ : pitch angle  $\theta$  [Colour figure can be viewed at [wileyonlinelibrary.com](http://wileyonlinelibrary.com)]

## 6.2 | Model validation

Because a significant inaccuracy on some derivatives relative to the phugoid mode is expected (see Section 3.6) and biases on the airspeed data fittings are observed in Section 6.1, the estimates  $C_{X_q}$ ,  $C_{X_{\delta_e}}$  are set to their a priori values. As mentioned in Section 3.6, in this way, low frequency errors might arise in the identified model, although standard feedback controls can easily handle such model mismatch.<sup>32</sup>

Furthermore, it turns out that the estimated derivative  $C_{Z_q}$ , ie, the force variation along the Z-axis, has no reasonable physical meaning, and for this reason, its value is fixed to the a priori estimate, too. Moreover, uncertainties on  $C_{Z_q}$  do not significantly deteriorate the predictive capability of the derived model.<sup>26</sup>

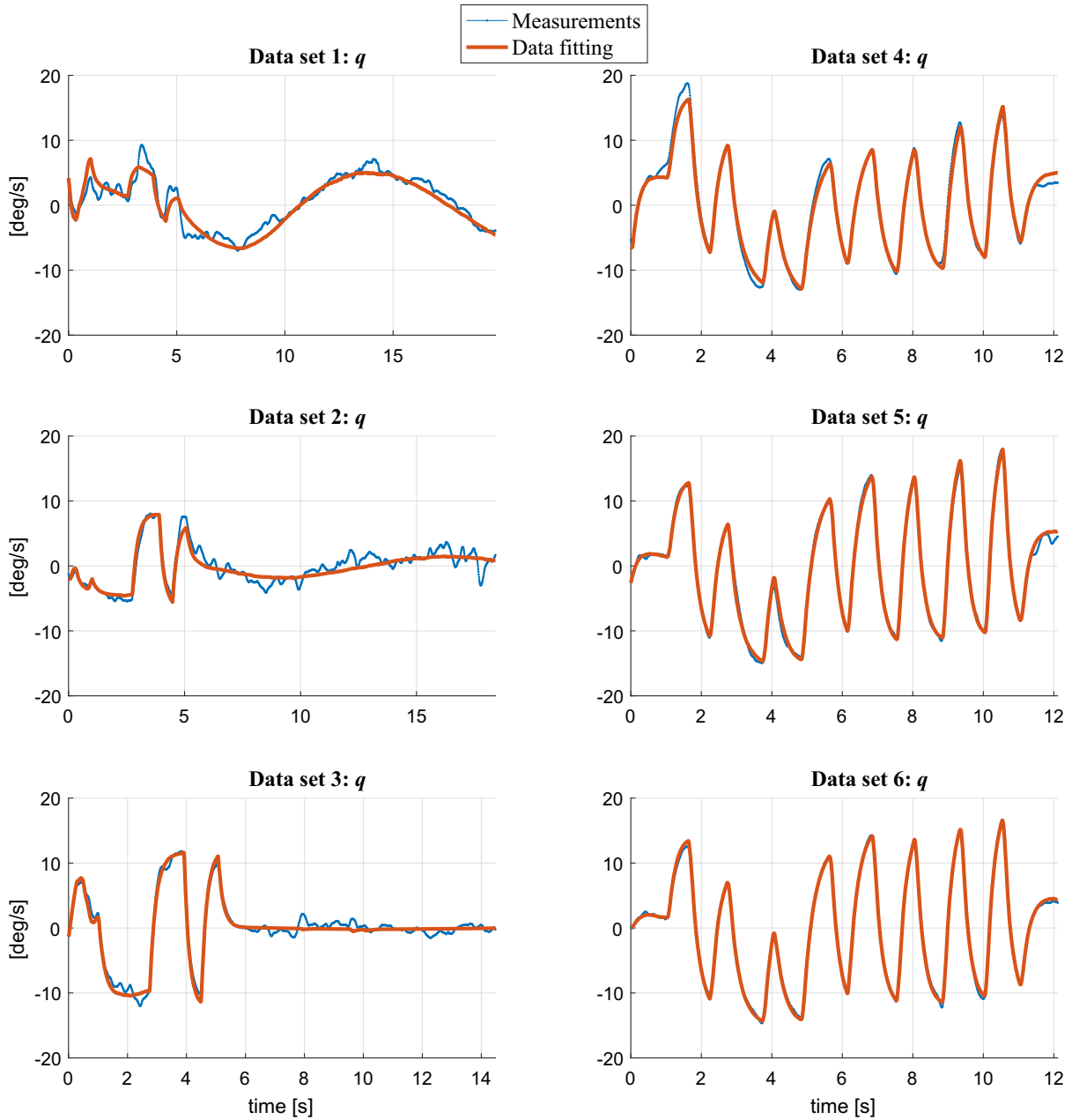


**FIGURE 15** Data fitting for multiple experiments along the longitudinal dynamics for  $V_{T_e} = 20\text{m/s}$ : pitch rate  $q$  [Colour figure can be viewed at [wileyonlinelibrary.com](http://wileyonlinelibrary.com)]

Table 4 collects the a priori  $\tilde{\mathbf{p}}$  and estimated  $\mathbf{p}^*$  dimensionless aerodynamic longitudinal derivatives augmented with the set of parameters  $\mathbf{p}_v$ , which are used for model validation, whereas Table 5 shows the corresponding identified phugoid and short-period mode.

In addition, in this case, a discrepancy is observed between the estimated phugoid period ( $P_o \approx 11$  seconds) and the observed one ( $P_o \approx 13$  seconds) in the airspeed responses shown in Figure 16.

The accuracy of an identified model is ultimately assessed via its capability to predict time responses.<sup>32</sup> For validation purpose, the identified model is simulated using a further flight test experiment shown in Figure 17. One can observe that the identified model provides a better fitting compared to the a priori one despite inaccuracies on the phugoid mode. Figure 18 shows the corresponding residual distributions  $\epsilon$  defined as

$$\epsilon_k = \hat{y}_k - \mathbf{h}(\mathbf{x}_k, \hat{\mathbf{u}}_k, \mathbf{p}_v), k = 1, \dots, N_v \quad (23)$$

**TABLE 3** Dimensionless aerodynamic longitudinal derivatives estimates carried out for different trimmed airspeed  $V_{T_e}$

| $V_{T_e}$                | 18 m/s  | 20 m/s  | 25 m/s  |
|--------------------------|---------|---------|---------|
| $C_{X_0}$                | -0.060  | 0.007   | -0.168  |
| $C_{X_\alpha}$           | -1.501  | -0.705  | -0.475  |
| $C_{X_q}$                | -30.202 | -20.799 | -4.852  |
| $C_{X_{\dot{\delta}_e}}$ | -0.396  | -0.952  | 0.804   |
| $C_{Z_0}$                | -0.478  | -0.483  | -0.494  |
| $C_{Z_\alpha}$           | -6.728  | -5.575  | -5.871  |
| $C_{Z_q}$                | -49.209 | -55.256 | -37.787 |
| $C_{Z_{\dot{\delta}_e}}$ | -1.668  | -0.823  | -1.145  |
| $C_{m_0}$                | 0.060   | 0.059   | 0.047   |
| $C_{m_\alpha}$           | -0.737  | -0.764  | -0.786  |
| $C_{m_q}$                | -18.504 | -20.335 | -15.911 |
| $C_{m_{\dot{\delta}_e}}$ | -0.966  | -0.971  | -0.865  |

**TABLE 4** Collection of the a priori  $\tilde{\mathbf{p}}$  and estimated  $\mathbf{p}^*$  dimensionless aerodynamic longitudinal derivatives.  $\mathbf{p}_v$  is the set of parameters chosen for model validation

| $\mathbf{p}$             | $\tilde{\mathbf{p}}$ | $\mathbf{p}^*$ | $\mathbf{p}_v$ |
|--------------------------|----------------------|----------------|----------------|
| $C_{X_0}$                | -0.033               | 0.007          | 0.007          |
| $C_{X_\alpha}$           | 0.409                | -0.705         | -0.705         |
| $C_{X_q}$                | -0.603               | -20.799        | -0.603         |
| $C_{X_{\dot{\delta}_e}}$ | -0.011               | -0.952         | -0.011         |
| $C_{Z_0}$                | -0.528               | -0.483         | -0.483         |
| $C_{Z_\alpha}$           | -4.225               | -5.575         | -5.575         |
| $C_{Z_q}$                | -7.500               | -55.256        | -7.500         |
| $C_{Z_{\dot{\delta}_e}}$ | -0.310               | -0.823         | -0.823         |
| $C_{m_0}$                | -0.031               | 0.059          | 0.059          |
| $C_{m_\alpha}$           | -0.607               | -0.764         | -0.764         |
| $C_{m_q}$                | -11.300              | -20.335        | -20.335        |
| $C_{m_{\dot{\delta}_e}}$ | -1.420               | -0.971         | -0.971         |

**TABLE 5** Identified longitudinal modes

| Mode       | Short-period | Phugoid | Unit  |
|------------|--------------|---------|-------|
| $\omega_n$ | 5.548        | 0.587   | rad/s |
| $\tau$     | 0.180        | 1.704   | s     |
| $\delta$   | 0.843        | 0.036   | —     |
| $S_{\%}$   | 0.721        | 89.210  | %     |
| $P_O$      | 2.108        | 10.712  | s     |

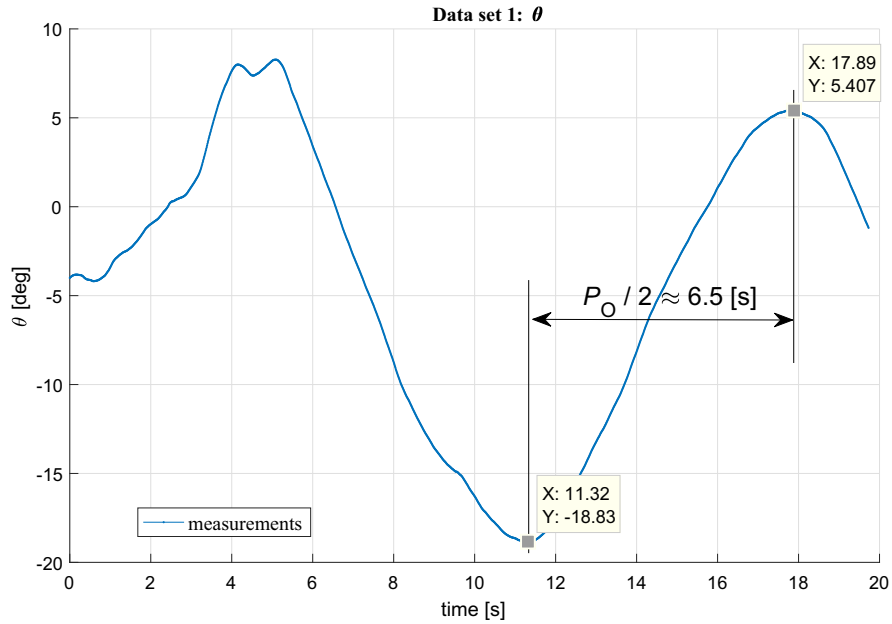


**FIGURE 16** Observed Phugoid period of oscillation  $P_O$  [Colour figure can be viewed at wileyonlinelibrary.com]

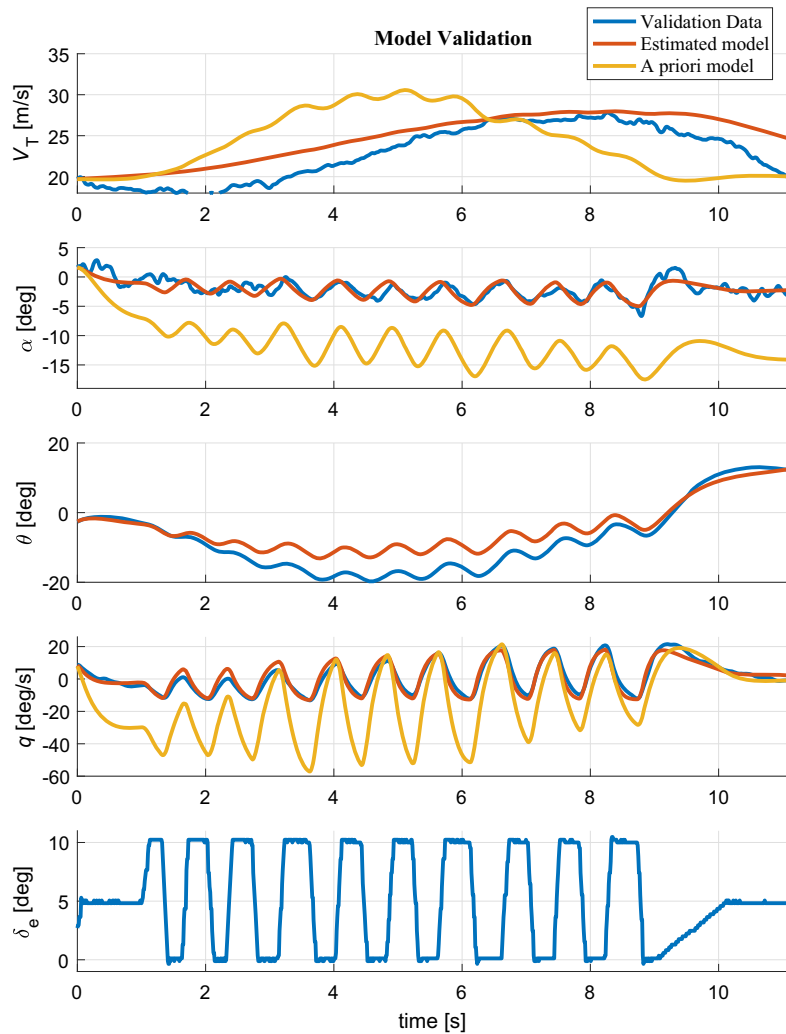


**FIGURE 17** Model structure assessment via validation data set. The a priori pitch angle  $\theta$  response is not shown due to its large deviation w.r.t. the obtained experimental values [Colour figure can be viewed at wileyonlinelibrary.com]

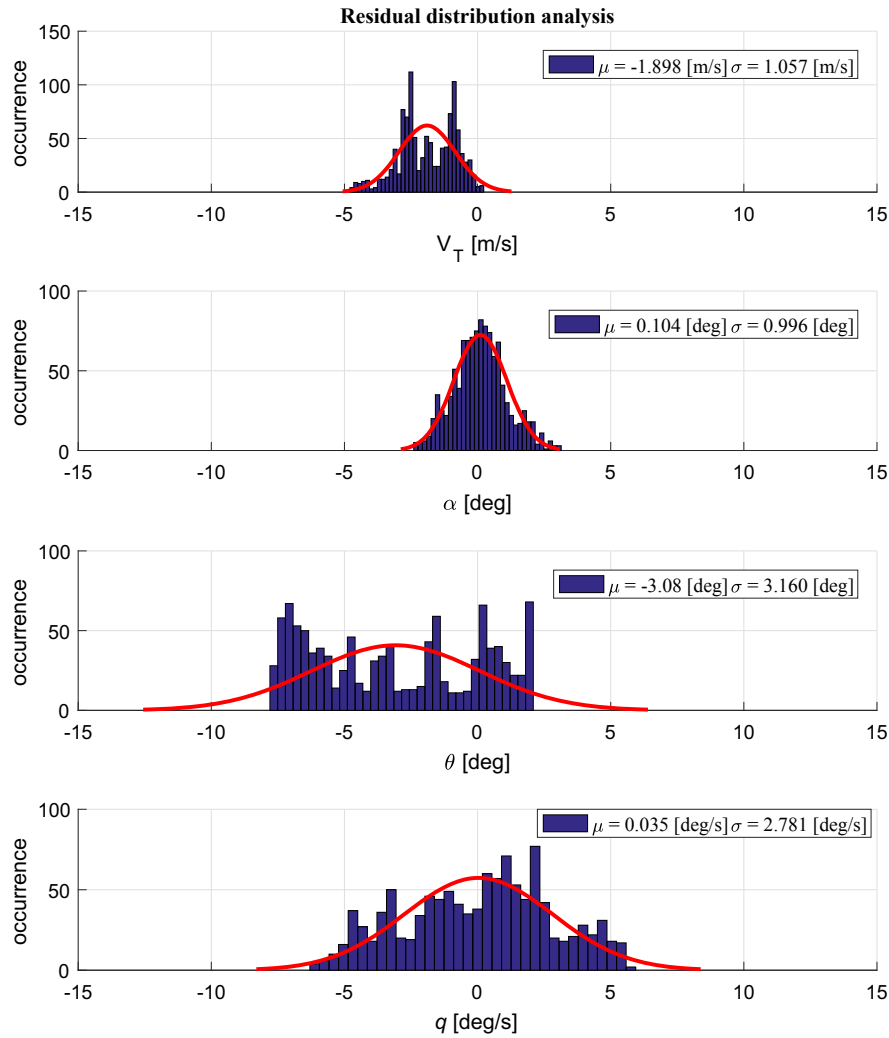


**FIGURE 18** Residual distribution analysis validation data set with corresponding mean value  $\mu$  and standard deviation  $\sigma$  [Colour figure can be viewed at [wileyonlinelibrary.com](http://wileyonlinelibrary.com)]

**TABLE 6** Theil inequality coefficients

|     | $V_T$ | $\alpha$ | $\theta$ | $q$  |
|-----|-------|----------|----------|------|
| TIC | 0.04  | 0.20     | 0.21     | 0.15 |

with  $N_v$  being the number of samples related to the validation data set. Practically speaking, the residual is the part of the data that the model is not able to reproduce; the aim is to achieve a residual resembling a white noise signal. However, it is well known that the residuals will not be white noise if the real system has significant process noise (atmospheric turbulence).<sup>5</sup>

Finally, estimation results are assessed via the so-called Theil inequality coefficient (TIC), which is defined by the following relationship<sup>34</sup>:

$$\text{TIC} = \frac{\sqrt{\frac{1}{N_v} \sum_{i=1}^{N_v} (\hat{y}_i - \mathbf{h}(\mathbf{x}_i, \hat{\mathbf{u}}_i, \mathbf{p}_v))^2}}{\sqrt{\frac{1}{N_v} \sum_{i=1}^{N_v} \hat{y}_i^2 + \sqrt{\frac{1}{N_v} \sum_{i=1}^{N_v} \mathbf{h}(\mathbf{x}_i, \hat{\mathbf{u}}_i, \mathbf{p}_v)^2}}}}. \quad (24)$$

The TIC provides a basis of judgment regarding the degree of predictability of a mathematical (estimated) model via a normalized metric between 0 and 1. A value of  $\text{TIC} = 0$  denotes a perfect match, whereas  $\text{TIC} = 1$  indicates the worst case scenario, ie, the mathematical model is not able to explain any of the data. Values of  $\text{TIC} \leq 0.25$  correspond to accurate prediction for rigid-wing aircraft.<sup>42,51</sup> Table 6 summarizes the TIC values for this work.

The results show that the angle of attack  $\alpha$ , pitch angle  $\theta$ , and pitch rate  $q$  are captured with high accuracy as well as the airspeed response  $V_T$  despite the uncertainties mentioned previously.

## 7 | CONCLUSIONS

In this paper, real flight test experiments and a subsequent time-domain MBPE have been carried out for a high lift, rigid-wing autonomous aircraft deployed for an AWES. A suitable and comprehensive nonlinear mathematical model for system identification purposes was introduced and the underlying model assumptions were discussed. Furthermore, an overview of the flight test procedure for a high lift autonomous aircraft has been provided. The experimental data sets were obtained for the longitudinal dynamics for the steady-state wing-level trim condition. In order to obtain the required estimation accuracy, aerodynamic derivatives were estimated within one single optimization problem, which takes into account all collected data carried out by both conventional 3-2-1-1 and optimized maneuvers. Finally, the identified model was assessed by time-domain model validation, residual distribution analysis, and TIC.

Experimental results have shown that system identification via real flight tests is able to improve the predictive capability of low fidelity a priori models for a high lift, rigid-wing aircraft. However, baseline models are equally important to deal with nonidentifiable dynamics as well as for designing maneuvers for system identification purposes.

Future work will aim toward the implementation of parameter estimation algorithms, which might further improve robustness w.r.t. turbulence effects, eg, the Filter-Error method.<sup>52</sup>

## ACKNOWLEDGEMENTS

The authors would like to thank Ampyx Power B.V. and in particular the flight operations team for conducting the system identification flight tests. This research was supported by the EU via FP7-ITN-TEMPO (607 957) and H2020-ITN-AWESCO (642 682), by the Federal Ministry for Economic Affairs and Energy (BMWi) via eco4wind and DyConPV, by the Deutsche Forschungsgemeinschaft (DFG) via Research Unit FOR 2401, and by the State Ministry of Baden-Wuerttemberg for Sciences, Research and Arts (Az: 22-7533.-30-20/9/3).

## ORCID

Giovanni Licitra  <https://orcid.org/0000-0003-0585-0189>

## REFERENCES

1. Loyd ML. Crosswind kite power (for large-scale wind power production). *J Energy*. 1980;4(3):106-111.
2. Ruiterkamp R, Sieberling S. Description and preliminary test results of a six degrees of freedom rigid wing pumping system. In: *Airborne Wind Energy*. Berlin, Germany: Springer-Verlag; 2013.
3. Gros S, Diehl M. Modeling of airborne wind energy systems in natural coordinates. In: *Airborne Wind Energy*. Berlin, Germany: Springer-Verlag; 2013:181-203.
4. Koenemann J, Williams P, Sieberling S, Diehl M. Modeling of an airborne wind energy system with a flexible tether model for the optimization of landing trajectories. *IFAC-PapersOnLine*. 2017;50(1):11944-11950.
5. Licitra G, Williams P, Gillis J, et al. Aerodynamic parameter identification for an airborne wind energy pumping system. *IFAC-PapersOnLine*. 2017;50(1):11951-11958.
6. Leloup R, Roncin K, Bles G, Leroux B, Jochum C, Parlier Y. Estimation of the lift-to-drag ratio using the lifting line method: application to a leading edge inflatable kite. In: *Airborne Wind Energy*. Berlin, Germany: Springer-Verlag; 2013:339-355.
7. Fasel U, Keidel D, Molinari G, Ermanni P. Aerostructural optimization of a morphing wing for airborne wind energy applications. *Smart Mater Struct*. 2017;26(9). <https://doi.org/10.1088/1361-665X/aa7c87>
8. Coleman J, Ahmad H, Pican E, Toal D. Non-reversing generators in a novel design for pumping mode airbornewind energy farm. In: *Airborne Wind Energy*. Berlin, Germany: Springer-Verlag; 2013:587-597.
9. Ampyx Power. Airborne Wind Energy. <https://www.ampyxpower.com>. Accessed February 6, 2018.
10. Makani. <https://x.company/makani/>. Accessed February 6, 2018.
11. TwingTec. Wind Energy 2.0. <http://twingtec.ch/>. Accessed February 6, 2018.
12. Kitemill. <http://www.kitemill.com/>. Accessed February 6, 2018.
13. e-kite. <http://www.e-kite.com/>. Accessed February 6, 2018.

14. Anderson JD. *Fundamentals of Aerodynamics*. 6th ed. New York, NY: McGraw-Hill; 2017.
15. Hoak DE, Finck RD. *USAF Stability and Control DATCOM*. Technical Report. Springfield, VA: National Technical Information Service; 1975.
16. Diehl M. Airborne wind energy: basic concepts and physical foundations. In: *Airborne Wind Energy*. Berlin, Germany: Springer-Verlag; 2013.
17. Ampyx Power B.V. Working principle. <https://www.youtube.com/watch?v=32CYqjoRnYY>. Accessed February 6, 2018.
18. Licitra G, Bürger A, Williams P, Ruitkamp R, Diehl M. Optimum experimental design of a rigid wing AWE pumping system. Paper presented at: IEEE 56th Conference on Decision and Control (CDC); 2017; Melbourne, Australia.
19. Licitra G, Bürger A, Williams P, Ruitkamp R, Diehl M. Optimal input design for autonomous aircraft. *J Control Eng Pract*. 2017;77:15-27.
20. Licitra G, Sieberling S, Engelen S, Williams P, Ruitkamp R, Diehl M. Optimal control for minimizing power consumption during holding patterns for airborne wind energy pumping system. Paper presented at: 2016 European Control Conference (ECC); 2016; Aalborg, Denmark.
21. Licitra G, Koenemann J, Horn G, Williams P, Ruitkamp R, Diehl M. Viability assessment of a rigid wing airborne wind energy pumping system. Paper presented at: 21st International Conference on Process Control (PC); 2017; Štrbské Pleso, Slovakia.
22. Williams P, Lansdorp B, Ockels W. Modeling and control of a kite on a variable length flexible inelastic tether. Paper presented at: AIAA Modeling and Simulation Technologies Conference and Exhibit, Guidance, Navigation, and Control and Co-located Conferences; 2007; Hilton Head, SC.
23. Williams P, Lansdorp B, Ruitkamp R, Ockels W. Modeling, simulation, and testing of surf kites for power generation. Paper presented at: AIAA Modeling and Simulation Technologies Conference and Exhibit, Guidance, Navigation, and Control and Co-located Conferences; 2008; Honolulu, HI.
24. Diehl M, Schmehl R, Ahrens U. *Airborne Wind Energy*. Berlin, Germany: Springer-Verlag; 2013. *Green Energy and Technology*. <https://doi.org/10.1007/978-3-642-39965-7>
25. Stevens BL, Lewis FL, Johnson EN. *Aircraft Control and Simulation: Dynamics, Controls Design, and Autonomous Systems*: Wiley; 2015. <https://doi.org/10.1002/9781119174882>
26. Mulder JA, Van Staveren WHJJ, Der Vaart JC. *Flight Dynamics (Lecture Notes)*. Delft, The Netherlands: TU Delft; 2000.
27. Etkin B. *Dynamics of Atmospheric Flight*. New York, NY: Wiley; 1972.
28. Goman M, Khrabrov A. State-space representation of aerodynamic characteristics of an aircraft at high angles of attack. *J Aircr*. 1994;31(5):1109-1115.
29. De Jong RC, Mulder JA. Accurate estimation of aircraft inertia characteristics from a single suspension experiment. *J Aircr*. 1987;24(6):362-370.
30. Lyons D. Obtaining optimal results with filar pendulums for moment of inertia measurements. *Weight Eng*. 2002;62(2):5-20.
31. Söderström T, Stoica P. Instrumental variable methods for system identification. *Circuits Syst Signal Process*. 2002;21(1):1-9. <https://doi.org/10.1007/BF01211647>
32. Dorobantu A, Murch A, Mettler B, Balas G. System identification for small, low-cost, fixed-wing unmanned aircraft. *J Aircr*. 2013;50(4):1117-1130.
33. Morelli EA, Klein V. Optimal input design for aircraft parameter estimation using dynamic programming principles. Paper presented at: AIAA Atmospheric Flight Mechanics Conference; 1990; Portland, OR.
34. Cook M. *Flight Dynamics Principles: A Linear Systems Approach to Aircraft Stability and Control*. 3rd ed. Oxford, UK: Elsevier Butterworth-Heinemann; 2013. <https://doi.org/10.1017/S0001924000010873>
35. McRuer DT, Graham D, Ashkenas I. *Aircraft Dynamics and Automatic Control*. Princeton, NJ: Princeton University Press; 2014.
36. Koehler R, Wilhelm K. Auslegung von Eingangssignalen für die Kennwertermittlung. Brunswick, Germany: DFVLR; 1977.
37. Mulder JA, Sridhar JK, Breeman JH. *Identification of Dynamic System - Applications to Aircraft. Part 2: Nonlinear Analysis and Manoeuvre Design*. Neuilly-sur-Seine, France: Advisory Group for Aerospace Research and Development (AGARD); 1994.
38. Marchand M. Untersuchung der Bestimmbarkeit der Flugmechanischen Derivative des CCV-Versuchsträgers F-104 G. Brunswick, Germany: DFVLR; 1977.
39. Ampyx Power B.V. Optimal system identification flight test. <https://www.youtube.com/watch?v=KBq5TTTOqf8>. Accessed February 6, 2018.
40. Versteeg HK, Malalasekera W. *An Introduction to Computational Fluid Dynamics: The Finite Volume Method*. Reading, MA: Addison-Wesley-Longman; 1995.
41. Morelli E. *Practical Input Optimization for Aircraft Parameter Estimation Experiments*. Hampton, VA: Langley Research Center, National Aeronautics and Space Administration; 1993.
42. Tischler MB, Remple RK. *Aircraft and Rotorcraft System Identification*. Reston, VA: American Institute of Aeronautics and Astronautics; 2006. *AIAA Education Series*. <https://doi.org/10.2514/4.868207>
43. Morelli EA. Practical aspects of the equation-error method for aircraft parameter estimation. Paper presented at: AIAA Atmospheric Flight Mechanics Conference and Exhibit, Guidance, Navigation, and Control and Co-located Conferences; 2006; Keystone, CO.
44. Ljung L. *System Identification: Theory for the User*. Upper Saddle River, NJ: Prentice Hall PTR; 1999.
45. Diehl M. Modeling and system identification. 2017.
46. Bock HG, Plitt KJ. A multiple shooting algorithm for direct solution of optimal control problems. Paper presented at: 9th IFAC World Congress: A Bridge Between Control Science and Technology; 1984; Budapest, Hungary.

47. Bock HG, Carraro T, Jäger W, Körkel S, Rannacher R, Schlöder J. *Model Based Parameter Estimation: Theory and Applications*. Berlin, Germany: Springer Science+Business Media; 2013.
48. Andersson JAE, Gillis J, Horn G, Rawlings JB, Diehl M. CasADi – a software framework for nonlinear optimization and optimal control. *Math Program Comput*. 2018. In press.
49. Wächter A, Biegler LT. On the implementation of an interior-point filter line-search algorithm for large-scale nonlinear programming. *Math Program*. 2006;106(1):25-57.
50. The Science and Technology Facilities Council. HSL: a collection of Fortran codes for large scale scientific computation. 2017.
51. Jategaonkar R, Fischenberg D, Von Gruenhagen W. Aerodynamic modeling and system identification from flight data-recent applications at DLR. *J Aircr*. 2004;41(4):681-691.
52. Grauer JA, Morelli EA. A new formulation of the filter-error method for aerodynamic parameter estimation in turbulence. Paper presented at: AIAA Atmospheric Flight Mechanics Conference, AIAA AVIATION Forum; 2015; Dallas, TX.

**How to cite this article:** Licitra G, Bürger A, Williams P, Ruitkamp R, Diehl M. Aerodynamic model identification of an autonomous aircraft for airborne wind energy. *Optim Control Appl Meth*. 2019;1–26. <https://doi.org/10.1002/oca.2485>

## APPENDIX

**TABLE A1** Physical properties of the high lift, rigid wing, autonomous aircraft

| Name                    | Symbol    | Value | Unit                         |
|-------------------------|-----------|-------|------------------------------|
| Mass                    | m         | 36.8  | kg                           |
| Moment of inertia       | $J_x$     | 25    | $\text{kg} \cdot \text{m}^2$ |
| Moment of inertia       | $J_y$     | 32    | $\text{kg} \cdot \text{m}^2$ |
| Moment of inertia       | $J_z$     | 56    | $\text{kg} \cdot \text{m}^2$ |
| Cross moment of inertia | $J_{xz}$  | 0.47  | $\text{kg} \cdot \text{m}^2$ |
| Reference wing area     | S         | 3     | $\text{m}^2$                 |
| Reference wing span     | b         | 5.5   | m                            |
| Reference chord         | $\bar{c}$ | 0.55  | m                            |

**TABLE A2** A priori longitudinal dimensional aerodynamic derivatives ( $V_{T_e} = 20 \text{ m/s}$ )

| X-axis         | Value  | Z-axis                 | Value  | M-axis         | Value   |
|----------------|--------|------------------------|--------|----------------|---------|
| $X_V$          | -0.147 | $Z_V$                  | -0.060 | $M_V$          | 0.0     |
| $X_\alpha$     | 7.920  | $Z_\alpha/V_{T_e}$     | -4.400 | $M_\alpha$     | -6.180  |
| $X_q$          | -0.163 | $Z_q$                  | 0.896  | $M_q$          | -1.767  |
| $X_{\delta_e}$ | -0.232 | $Z_{\delta_e}/V_{T_e}$ | -0.283 | $M_{\delta_e}$ | -10.668 |

**TABLE A3** Sensors noise standard deviation  $\sigma_y$

| Sensor               | Variable               | $\sigma_y$ | Unit  |
|----------------------|------------------------|------------|-------|
| Five hole pitot tube | $V_T$                  | 1.0        | m/s   |
| Five hole pitot tube | $(\alpha, \beta)$      | 0.5        | deg   |
| IMU                  | $(\phi, \theta, \psi)$ | 0.1        | deg   |
| IMU                  | $(p, q, r)$            | 0.1        | deg/s |